Simulations of expected signal and background of gamma-ray sources by large field-of-view detectors aboard CubeSats

Gábor Galgóczi[a,b,*], **Jakub Řípa**[a,c,d,e,#], **Riccardo Campana**[f], **Norbert Werner**[e,g,c], **András Pál**[h], **Masanori Ohno**[a,c,g], **László Mészáros**[h], **Tsunefumi Mizuno**[i], **Norbert Tarcai**[j], **Kento Torigoe**[g], **Nagomi Uchida**[g], **Yasushi Fukazawa**[g], **Hiromitsu Takahashi**[g], **Kazuhiro Nakazawa**[k], **Naoyoshi Hirade**[g], **Kengo Hirose**[g], **Syohei Hisadomi**[k], **Teruaki Enoto**[l], **Hirokazu Odaka**[m], **Yuto Ichinohe**[n], **Zsolt Frei**[a], **László Kiss**[h]

[a]Eötvös University, Institute of Physics, Pázmány Péter sétány 1/A, Budapest, Hungary, 1117
[b]Wigner Research Centre, Konkoly-Thege Miklós út 29-33., Budapest, Hungary, 1121
[c]MTA-Eötvos University Lendület Hot Universe Research Group, Pázmány Péter sétány 1/A, Budapest, Hungary, 1117
[d]Charles University, Faculty of Mathematics and Physics, Astronomical Institute, V Holešovičkách 2, Prague 8, Czech Republic, 180 00
[e]Masaryk University, Faculty of Science, Department of Theoretical Physics and Astrophysics, Kotlářská 2, Brno, Czech Republic, 611 37
[f] INAF - Astrophysical and Space Science Observatory (OAS), Via Gobetti 101, Bologna, Italy, 40129
[g]Hiroshima University, School of Science, 1-3-1 Kagamiyama, Higashi-Hiroshima, Japan, 739-8526
[h]Konkoly Observatory of the Hungarian Academy of Sciences, Konkoly-Thege ut 15-17, Budapest, Hungary, 1121
[i]Hiroshima University, Hiroshima Astrophysical Science Center, 1-3-1 Kagamiyama, Higashi-Hiroshima, Japan, 739-8526
[j]C3S Electronics Development LLC., Könyves Kálmán krt. 12-14., Budapest, Hungary, 1097
[k]Nagoya University, Department of Physics, Furo-cho, Chikusa-ku, Nagoya, Aichi, Japan, 464-8602
[l]Kyoto University, The Hakubi Center for Advanced Research and Department of Astronomy, Kyoto, Japan, 606-8302
[m]University of Tokyo, Department of Physics, 7-3-1 Hongo, Bunkyo, Tokyo, Japan, 113-0033
[n]Rikkyo University, Department of Physics, Nishi Ikebukuro 3-34-1, Toshimaku, Tokyo, Japan, 171-8501

Abstract. In recent years the number of CubeSats (U-class spacecrafts) launched into space has increased exponentially marking the dawn of the nanosatellite technology. In general these satellites have a much smaller mass budget compared to conventional scientific satellites which limits shielding of scientific instruments against direct and indirect radiation in space.

In this paper we present a simulation framework to quantify the signal in large field-of-view gamma-ray scintillation detectors of satellites induced by X-ray/gamma-ray transients, by taking into account the response of the detector. Furthermore, we quantify the signal induced by X-ray and particle background sources at a Low-Earth Orbit outside South Atlantic Anomaly and polar regions. Finally, we calculate the signal-to-noise ratio taking into account different energy threshold levels. Our simulation can be used to optimize material composition and predict detectability of various astrophysical sources by CubeSats.

We apply the developed simulation to a satellite belonging to a planned *CAMELOT* CubeSat constellation. This project mainly aims to detect short and long gamma-ray bursts (GRBs) and as a secondary science objective, to detect soft gamma-ray repeaters (SGRs) and terrestrial gamma-ray flashes (TGFs). The simulation includes a detailed computer-aided design (CAD) model of the satellite to take into account the interaction of particles with the material of the satellite as accurately as possible.

Results of our simulations predict that CubeSats can complement the large space observatories in high-energy astrophysics for observations of GRBs, SGRs and TGFs. For the detectors planned to be on board of the *CAMELOT* CubeSats the simulations show that detections with signal-to-noise ratio of at least 9 for median GRB and SGR fluxes are achievable.

Keywords: Geant4, GRB, gamma-rays, satellite, cosmic background.

*Gábor Galgóczi, galgoczi@caesar.elte.hu **#Jakub Řípa,** jakub.ripa@ttk.elte.hu

arXiv:2102.08104v3 [astro-ph.IM] 2 May 2021

1 Introduction

Particle background is a considerable constraint for satellites, particularly those aiming to investigate the high-energy Universe. It is especially important for instruments without an anti-coincidence shield, e.g. for the increasingly large number of CubeSats which have recently been proposed for scientific missions.

A dedicated Geant4[1] software has been developed including the simulation of the optical light propagation inside the scintillators used as detectors. This way the detector response can be taken into account. In order to include the effects of scattering, photon conversion and other interactions happening between background particles, X-ray photons and the materials of the satellite, a computer-aided design (CAD) model of the whole satellite was included in the simulations.

The spectra of high energy photons and particles which contribute to the overall detected background were used as an input to the Geant4 simulations. These components of the external background include cosmic X-rays/γ-rays, cosmic ray particles, geomagnetically trapped particles and albedo (secondary) particles produced in the Earth's atmosphere.

In order to validate the background simulations, a set of dedicated experiments were carried out at the Hiroshima University in order to obtain the scintillator optical parameters (e.g. reflectivity of the surfaces and absorption length) which determine the position dependence of signal collection efficiency.

The developed simulation, spectra of the X/γ-rays and particle background as well as example spectra of high-energy photon transients were applied on one 3U CubeSat belonging to the planned Cubesats Applied for MEasuring and LOcalising Transients (*CAMELOT*) constellation.[2–4] This simulation framework can be also helpful for other CubeSat and SmallSat missions

with gamma-ray detectors in preparation by other teams, e.g. *BurstCube*,[5,6] *BlackCAT*,[7] Gravitational wave high-energy Electromagnetic Counterpart All-sky Monitor (*GECAM*),[8] Gamma-Ray Integrated Detectors (GRID),[9] *Glowbug*,[10] High Energy Rapid Modular Ensemble of Satellites - Scientific Pathfinder (*HERMES-SP*),[11] Satellite Polarimeter for High eNergy X-rays (*SPHiNX*),[12] *SkyHopper*[1], Space Industry Responsive Intelligent Thermal satellite, (*SpIRIT*)[2].

The paper is organized as follows: Sec. 2 describes the astrophysical sources whose detectability is investigated, Sec. 3 overviews various background components, Sec. 4 describes the *CAMELOT* satellites and the detector system, Sec. 5 details the validation of Geant4 simulations and the calibration of the detector's optical parameters, Sec. 6 describes the performed Geant4 simulations, Sec. 7 presents the results of Geant4 simulations and Sec. 9 summarizes the conclusions.

2 Expected X-ray/γ-ray Transient Sources

The main scientific objective of the proposed *CAMELOT* satellites is the detection of GRBs.[13,14] Short GRBs (sGRBs) originate from a merger of two neutron stars and possibly also from a merger of a neutron star and a black hole.[15–18] The typical duration T_{90} (the time during which the cumulative counts increase from 5 % to 95 %) of their prompt gamma-ray emission is $\lesssim 2\,\mathrm{s}$ in the observer frame[19] and their gamma-ray energy flux peaks at $\sim 600\,\mathrm{keV}$. Long GRBs (lGRBs) originate in the gravitational collapse of fast-spinning massive stars and their typical duration is $\gtrsim 2\,\mathrm{s}$. The prompt spectra of lGRBs are on average softer then the sGRB spectra with their energy flux peaking at $\sim 200\,\mathrm{keV}$.

The *CAMELOT* satellites might be sensitive also to other astrophysical X-ray transients such as soft gamma repeaters with typical duration of individual peaks in their light curves $\sim 0.2\,\mathrm{s}$ and

---

[1] https://skyhopper.research.unimelb.edu.au
[2] https://spirit.research.unimelb.edu.au

with X-ray energy flux peaking at around 20 keV (see Sec. 2.2). Note that a hard component above 100 keV has been observed as well.[20,21] Also the gamma-ray phenomena produced in the Earth's atmosphere during thunderstorms[22] called terrestrial gamma-ray flashes might be observed. These events are typically shorter than 1 ms and have gamma-ray spectra reaching energies of several MeV.[23] The following subsections describe in detail the fluxes expected from these sources. Fig. 1 summarizes the spectra of the X-ray/γ-ray transient sources which we study in this paper.
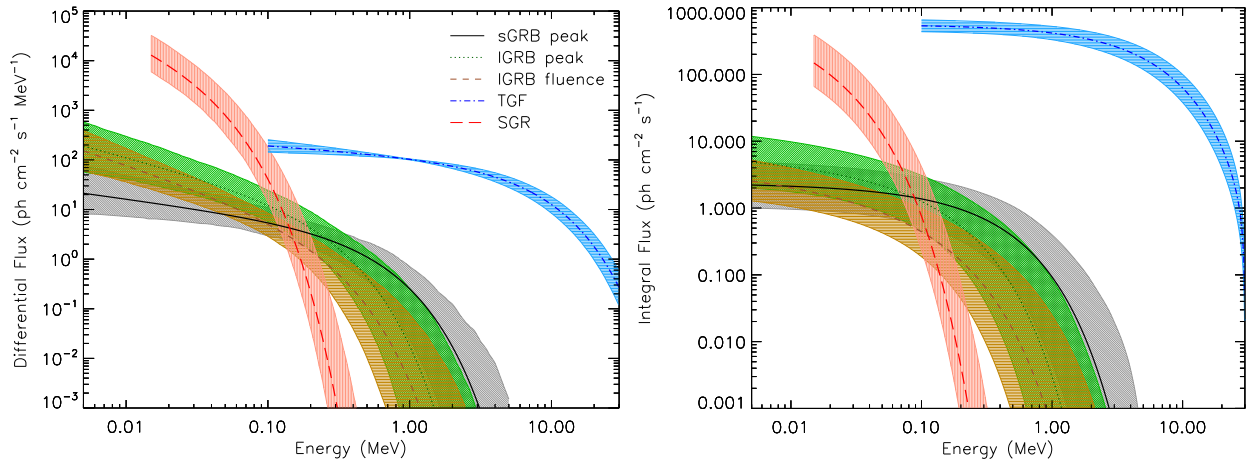

Fig 1 Differential (left) and integral (right) spectra of typical GRBs, SGR and TGF. The black solid curve shows a typical peak spectrum of a sGRB. The black dotted curve shows a typical peak spectrum of a lGRB and the black dashed line shows a typical fluence spectrum of a lGRB accumulated over the duration of the burst. The blue solid curve shows an average spectrum of a TGF based on measurements from the *AGILE* satellite. The red solid curve shows a typical spectrum of a burst from a SGR based on measurements from the Konus experiment. The shaded regions correspond to 68 % CL.

2.1 Typical Short and Long Gamma-Ray Burst Spectra

Since the main objective of the *CAMELOT* mission is the detection of GRBs, we run Monte Carlo (MC) simulations using the typical spectra of sGRBs and lGRBs in order to estimate the expected signal-to-noise ratio. The typical spectra were constructed using the *Fermi* GBM Burst Catalog (FERMIGBRST[3]). For detailed information about the catalog see Ref. 24–27. For sGRBs, we used the so called peak flux spectrum which is accumulated over the peak of the GRB (typically

---

[3]https://heasarc.gsfc.nasa.gov/W3Browse/fermi/fermigbrst.html

over 64 ms or 1024 ms). In case of lGRBs, we used the peak flux spectrum and the so called fluence spectrum, which is accumulated over the whole duration of the burst.

Note that the 64, 256 and 1024 ms timescales of measured peak fluxes reported in the catalog do not match all the trigger timescales used by *Fermi*/GBM. The triggering system employs 120 possible sets of trigger algorithms (not all actively employed at a time and approximately 60 trigger algorithms are currently active[27]) consisting of eight set of energy bands, ten time scales 16, 32, 64, 128, 256, 512, 1024, 2048, 4096, 8192 ms and different time offsets for two phases of selected time interval. Most frequently, GBM triggers on 5 time scales from 16 to 4096 ms.[26]

The typical spectra of sGRB and lGRB were constructed in the following way. First, we checked what was the most common best fit spectral model in the catalog. For peak flux spectra of sGRBs it was the power law model (PL). For the peak flux and fluence spectra of lGRBs it was the Comptonized model (CPL, exponential cutoff power law). For detailed information about the different spectral models see Ref. 24.

Although PL model was the most frequent one for peak spectra of sGRBs in the FERMIGBRST catalog, we use the second most frequent model, i.e. CPL. The reason is that sGRBs dim in peak flux are most frequently best fit by PL whereas brighter sGRBs are most frequently fit by CPL model. A likely explanation is that short GRB have Comptonized spectra, and that weak sGRBs produce insufficient signal in the instrument to distinguish the models.

Then in case of the peak spectra, we used the median best fit spectral parameters and then we tuned the normalizations A of the spectra to obtain the values of the integral fluxes in the range of $10 - 1000$ keV equal to the median 1024 ms, 256 ms and 64 ms timescale peak fluxes obtained from the catalog. The median peak fluxes for sGRBs for 1024 ms, 256 ms and 64 ms time scales and in the $10 - 1000$ keV range are 2.0, 4.8 and 7.5 ph cm^{-2}s^{-1}, respectively. Note that the median

power law index for PL model for sGRBs peak spectra is $\alpha = -1.4$ which is unphysical[28] and that is also the reason why we use CPL model for sGRB spectra. In case of lGRBs the median peak fluxes for 1024 ms, 256 ms and 64 ms time scales and in the same energy range are 4.1, 5.2 and 6.7 ph cm^{-2}s^{-1}, respectively. For the fluence spectra of lGRBs, we used the median best fit spectral parameters, including the normalization, from the catalog. The obtained spectral parameters are in Table 1. The pivot energy E_{piv} is fixed at 100 keV. Figure 1 shows the typical GRB spectra with shaded regions corresponding to 68 % CL. These 68 % CL were obtained from the measured spectral parameters separately for short and long GRBs in the FERMIGBRST catalog and using the CPL spectral model.

Table 1 Spectral parameters of typical GRB spectra.

GRB type	Spec. type	A_{1024}	A_{256}	A_{64}	A	α	E_{peak} (keV)
sGRB	pflx	$0.0068^{+0.0090}_{-0.0035}$	$0.016^{+0.021}_{-0.008}$	$0.025^{+0.033}_{-0.013}$	—	$-0.38^{+0.34}_{-0.30}$	669^{+574}_{-350}
lGRB	pflx	$0.020^{+0.036}_{-0.012}$	$0.026^{+0.045}_{-0.015}$	$0.033^{+0.058}_{-0.019}$	—	$-0.75^{+0.37}_{-0.30}$	235^{+269}_{-117}
lGRB	flnc	—	—	—	$0.009^{+0.010}_{-0.004}$	$-0.96^{+0.37}_{-0.31}$	183^{+250}_{-89}

The spectral parameters are for the peak flux spectra (pflx) and the fluence spectra (flnc) of typical short and long GRBs. The normalizations A_{1024}, A_{256} and A_{64} are for the 1024 ms, 256 ms and 64 ms timescale peaks, respectively, A is the normalization for the fluence spectrum and all normalizations are in units of ph cm^{-2}s^{-1}keV^{-1}. Parameters α and E_{peak} are respectively the power law index and the peak energy of the Comptonized model. The uncertainties correspond to 68 % CL.

2.2 Soft Gamma Repeaters

Soft gamma repeaters and anomalous X-ray pulsars (AXPs) are believed to be neutron stars with extremely strong magnetic fields of up to $B \sim 10^{14} - 10^{15}$ G called "magnetars".[29–31] For reviews see Refs. 20, 32–34. First observations date to 1979[35] with several magnetar bursts detected up to now, see e.g. Refs. 21, 36–38. For example a giant flare of magnetar SGR 1806-20 on 27 December,

2004 was observed by several satellites[39–43] and it was so bright that it saturated detectors.

SGR giant flares are rare and it is essential for their better understanding to observe and monitor all of them. The all sky coverage provided by future networks of nano-satellites will ensure that all future SGR outbursts will be detected and their behaviour will be monitored.

The SGR spectra are in soft gamma-ray region and well represented by a single blackbody (BB) or two-temperature BB model.[21] Above ~ 30 keV the spectra are well modeled by optically thin thermal bremsstrahlung (OTTB).[32]

In our simulations we analyze the response to regular SGR bursts. For an example spectrum of a regular SGR we utilize the Konus catalog of SGRs detected from 1978 to 2000.[44] The catalog contains bursts from SGR 0526-66, 1627-41, 1801-23, 1806-20 and 1900+14 observed using detectors on board Venera 11–14, Wind, and Kosmos 2326 spacecrafts. The SGR photon spectra in the catalog are modeled by optically thin thermal bremsstrahlung using:

$$F(E) = AE^{-1}e^{-\frac{E}{kT}},\tag{1}$$

where kT (keV) is the spectral parameter, E (keV) is the photon energy and A (ph cm^{-2}s^{-1}) is the normalization factor.

We took 81 spectral fits from the catalog and derived the normalization factor A from each spectrum. Figure 2 shows the distribution of the kT parameter and the normalization A. The median values are $kT = 22^{+8}_{-3}$ keV and $A = 384^{+493}_{-300}$ ph cm^{-2}s^{-1}. The uncertainties correspond to 68 % CL. The typical duration of SGR bursts in the catalog is ~ 0.2 s. We use these parameters for an example SGR spectrum used in our MC simulations in the energy range of $15 - 500$ keV. The spectrum is shown in Figure 1 with the shaded region corresponding to 68 % CL which was

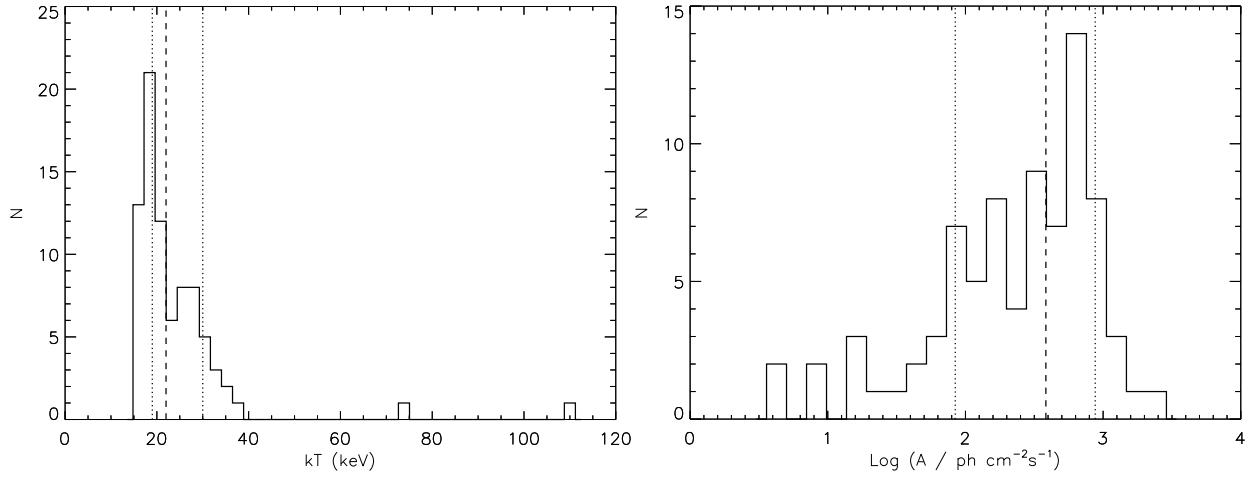calculated using MC simulations and the aforementioned values of kT and A parameters with their uncertainties.

Fig 2 Distribution of the spectral parameter kT (left) and normalization A (right) from the Konus SGR catalog[44] for 81 spectral fits. The dashed lines mark the median values and the regions delimited by dotted lines correspond to 68 % CL.

2.3 Terrestrial Gamma-Ray Flashes

Terrestrial gamma-ray flashes, brief bright bursts of multi-MeV gamma-rays, which are believed to be emitted by thunderclouds and generated, via bremsstrahlung, by the relativistic runaway electrons accelerated by electric fields in the atmosphere.[23] They were discovered by the Burst and Transient Source Experiment (BATSE) aboard Compton Gamma-ray Observatory (*CGRO*).[45] Plentiful observations have also been provided by other astrophysical instruments such as the Reuven Ramaty High Energy Solar Spectroscopic Imager (*RHESSI*),[46,47] the Gamma Ray Burst Monitor (GBM) on board the *Fermi* satellite,[48–50] and the Astrorivelatore Gamma ad Immagini Leggero (*AGILE*) satellite.[51–53] The *AGILE* satellite was launched to 550 km altitude with inclination of 2.5°. The Mini-Calorimeter (MCAL) is composed of 30 CsI(Tl) scintillator bars with each crystal of dimension of $15 \times 23 \times 375$ mm^3 giving the detector a sensitivity from 300 keV to 200 MeV and the effective area of $200 - 1200$ cm^2.[54] Although this makes *AGILE*/MCAL a more sensitive instru-

ment for TGF detection than what is foreseen for *CAMELOT*, which is expected to be launched to polar LEO with detectors composed of 5 mm thick CsI(Tl) crystals, we use the *AGILE*/MCAL observations of TGFs as a reference for our simulations because the mission accumulated a large and high quality TGF database in orbit. For their TGF observations see the 3rd *AGILE* TGF catalog[22,55] and the corresponding online catalog[4].

The duration of TGFs is typically below 1 ms with the peak of the distribution around $100 - 200\,\mu$s.[51–53] *AGILE* measurements show that the cumulative spectrum of 228 single-pulse TGFs in the range $0.4 - 30$ MeV can be fitted by a power law with exponential cutoff:[52]

$$F(E) = K \left(\frac{E}{1\,\text{MeV}} \right)^{-\alpha} e^{-\frac{E}{E_\text{C}}}, \tag{2}$$

where $\alpha = 0.20^{+0.12}_{-0.13}$ and $E_\text{C} = 5.5^{+0.7}_{-0.6}$ MeV. The cumulative spectrum is a rough approximation because of the effects due to atmospheric absorption from different source regions and due to the direction-dependent detector response which in the cumulative spectrum are smeared out. For analysis of instrumental effects and their impact on energy spectra see.[56]

The fluence distribution can be represented with a power law with an index of -2.2 to -2.4.[52,57] Therefore, there is no typical observed TGF fluence. However, for a reference we can consider a typical TGF fluence at the threshold level of *AGILE* which is around $0.05\,\text{ph}\,\text{cm}^{-2}$ over the full energy range of *AGILE*/MCAL $0.3 - 30$ MeV and this typical fluence is emitted over an average duration T_{50} of less than $100\,\mu s$ (M. Marisaldi, private communication).[53] The normalization K corresponding to this fluence integrated over $0.3 - 30$ MeV and within $100\,\mu s$ is $K = 123\,\text{ph}\,\text{cm}^{-2}\text{s}^{-1}\text{MeV}^{-1}$. We assume this normalization in our MC simulations. The spectrum

---

[4]https://www.ssdc.asi.it/mcal3tgfcat/

extrapolated to 100 keV is shown in Figure 1 with the shaded region corresponding to 68 % CL which was calculated using MC simulations and the aforementioned values of α and E_C parameters with their uncertainties. We assume that the published uncertainties of α and E_C correspond to 68 % CL. Normalization K was kept fixed because it corresponds to the fluence detection threshold of TGFs by *AGILE*.

3 Components of Cosmic, Albedo and Trapped Particle Radiation

There are several external background components at Low-Earth Orbits (LEO) which need to be considered in a study of the expected detected background count rate by an instrument with large field-of-view (FOV). The various components include extragalactic gamma-rays, cosmic-ray particles, secondary gamma-rays and particles produced in the Earth's atmosphere and the Galactic gamma emission. For overview see publications Refs. 58–70 and technical notes Refs. 71,72. The following subsections describe each component in detail and Fig. 3 shows a comparison of the in-orbit expected background fluxes which we use in our Geant4 simulations involving the mass model of one 3U *CAMELOT* CubeSat and its detectors.

3.1 *Cosmic X-ray/γ-ray Background*

The cosmic X-ray/γ-ray background (CXB) was discovered by a sounding rocket in 1962.[73] It is nearly isotropic emission detected over a wide range of energies from few keV to few 100 GeV.[60, 61, 63, 64, 66, 74–88] It is composed of high-energy emission from various extragalactic sources (active galactic nuclei, quasi-stellar objects, supernovae Ia, galaxy clusters, starburst galaxies, X-ray binaries, hot intergalactic gas).[61, 81, 84, 89–101] Some authors also argue that the diffuse γ-ray radiation originates in Cosmic Microwave Background[102] being inverse Compton scattered on cosmic-ray electrons.[103, 104]
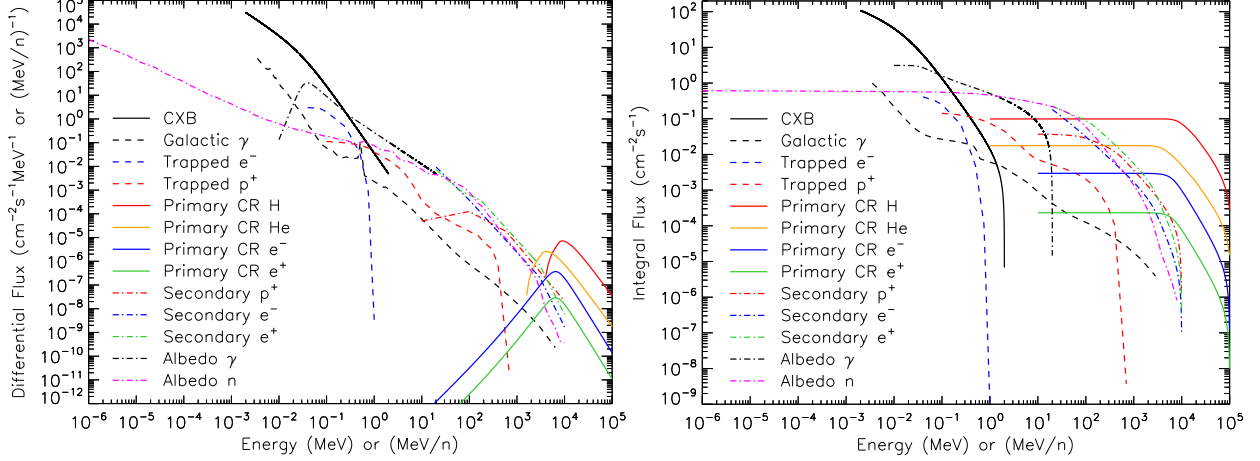
Fig 3 An overview of various background components. *Left:* The differential photon flux multiplied by the solid angles of the incident radiation valid for the expected altitude of the satellite of $500\,\mathrm{km}$ and for all-sky field-of-view. Trapped particle, primary CR H and He fluxes are for the orbital inclination $i = 20°$. Primary CR e$^-$ and e$^+$ fluxes are for the geomagnetic latitude $\theta_\mathrm{M} = 29.6°$. Secondary p$^+$ flux was obtained from the combination of data for $0.3\,\mathrm{rad} \leq \theta_\mathrm{M} \leq 0.4\,\mathrm{rad}$ and for $1.0 \leq$ L-shell ≤ 1.7, where L-shell is the McIlwain L-parameter. Secondary e$^-$ and e$^+$ fluxes were obtained from the combination of data for $0\,\mathrm{rad} \leq \theta_\mathrm{M} \leq 0.3\,\mathrm{rad}$ and for $1.0 \leq$ L-shell ≤ 1.2. Albedo γ flux is for $i = 20.6°$. Albedo n is for cutoff rigidity $R_\mathrm{cut} = 5\,\mathrm{GV}$ or $\theta_\mathrm{M} = 37°$. Details are described in Sec. 3. *Right:* The integral photon flux for the same models also multiplied by the same solid angles.

There are several empirical models used to describe the measured flux.[60,69,74,84,105] In our simulations we compare two models: the model introduced by Gruber et al. (1999)[105] and the one derived by Ajello et al. (2008)[84] (see Sec. 7).

The Gruber et al. (1999) model[105] fits the low-energy as well as the high-energy part of the CXB measurements obtained by *HEAO-1*,[106] *CGRO*/COMPTEL and *CGRO*/EGRET[107] instruments across a wide energy range spanning from $3\,\mathrm{keV}$ to $100\,\mathrm{GeV}$. This empirical model is used as a standard in modeling of the CXB flux for planning space missions. The differential photon flux $F(E) \equiv dN/dE$ in units of $\mathrm{ph\,cm^{-2}s^{-1}sr^{-1}keV^{-1}}$ is:

for energies $E = 3 - 60\,\mathrm{keV}$

$$F(E) = 7.877 \left(\frac{E}{1\,\mathrm{keV}} \right)^{-1.29} e^{-\frac{E}{41.13\,\mathrm{keV}}} \tag{3}$$

11

and for energies $E > 60\,\mathrm{keV}$ it is

$$F(E) = \frac{0.0259}{60}\left(\frac{E}{60\,\mathrm{keV}}\right)^{-6.5} + \frac{0.504}{60}\left(\frac{E}{60\,\mathrm{keV}}\right)^{-2.58} + \frac{0.0288}{60}\left(\frac{E}{60\,\mathrm{keV}}\right)^{-2.05}. \quad (4)$$

Ajello et al. (2008)[84] derived a CXB model which is in a good agreement with measurements from *Swift*/BAT,[84] *HEAO-1*,[105] *INTEGRAL*,[82] *BeppoSAX*[83] instruments and other missions in the $2\,\mathrm{keV} - 2\,\mathrm{MeV}$ energy range. The differential photon flux $F(E) \equiv dN/dE$ in units of $\mathrm{ph\,cm^{-2}s^{-1}sr^{-1}keV^{-1}}$ is:

$$F(E) = \frac{C}{(E/E_{\mathrm{B}})^{\Gamma_1} + (E/E_{\mathrm{B}})^{\Gamma_2}}, \quad (5)$$

where the parameters with $1\,\sigma$ errors are $C = (10.15 \pm 0.80) \times 10^{-2}$, $\Gamma_1 = 1.32 \pm 0.018$, $\Gamma_2 = 2.88 \pm 0.015$ and $E_{\mathrm{B}} = 29.99 \pm 1.1\,\mathrm{keV}$.

The CXB flux is omnidirectional and for $500\,\mathrm{km}$ altitude it irradiates a satellite from a solid angle of $8.64\,\mathrm{sr}$ ($3.93\,\mathrm{sr}$ are occulted by the Earth). The CXB spectra for different models, including the two previously discussed, are shown in Figure 4. The integral flux, i.e. the integrated flux for energies above a given energy threshold, for the Gruber et al. (1999) model[105] and for $E > 10\,\mathrm{keV}$ is $30.3\,\mathrm{ph\,cm^{-2}s^{-1}}$ whereas for the Ajello et al. (2008) model the integral flux at the same low-energy threshold is $33.7\,\mathrm{ph\,cm^{-2}s^{-1}}$.

Concerning the *CAMELOT* CubeSats, the detectors are $5\,\mathrm{mm}$ thick CsI(Tl) scintillators (as described in Sec. 4) with effective area having maximum at $\sim 100\,\mathrm{keV}$ (see Figure 18). The scintillator is relatively transparent to gamma-rays above $2\,\mathrm{MeV}$. For example the effective area at $1\,\mathrm{MeV}$ is a factor of about 7 lower than at $100\,\mathrm{keV}$. Although some gamma-rays can cause pair-production or Compton scatter in the material of the satellite and then lower-energy gamma-rays

can reach the scintillator, the CXB flux above 2 MeV is much lower than at few tens of keV or at 100 keV. Therefore, the high-energy gamma-ray component (above few MeV) included in the Gruber et al. (1999) model[105] is not essential for the *CAMELOT*'s detectors.

Ajello et al. (2008)[84] discusses that the normalization of the *Swift*/BAT CXB spectrum at 30 keV (CXB peak) is $\sim 8\,\%$ higher than the *HEAO-1*[105] measurement and consistent with the *INTEGRAL*[82] one. Also, the *HEAO-1* measurement has 10 % precision at the CXB peak. Therefore, we use both CXB models to simulate the expected detected background by *CAMELOT*, however, for a more detailed analysis, e.g. detected count rate as a function of energy threshold, we choose a more conservative approach and use the Ajello et al. (2008) model which gives $\sim 9\,\%$ higher integral flux in the energy range of $20 - 500\,\mathrm{keV}$, which is approximately the sensitivity range of *CAMELOT*'s detectors.
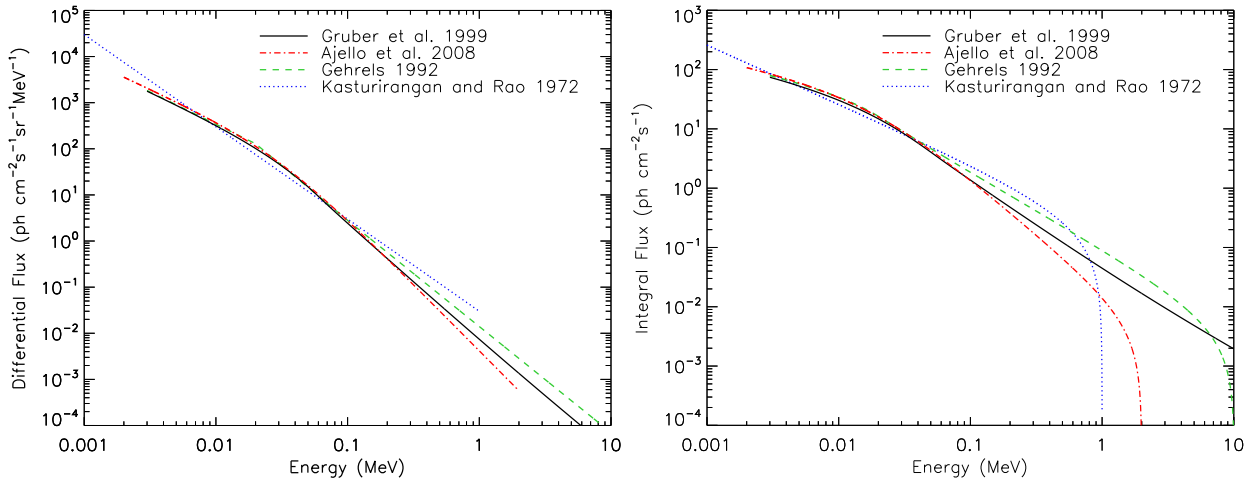

Fig 4 The CXB spectra for different models. *Left:* The differential photon flux. *Right:* The integral photon flux for the same models. The integral flux is multiplied by a solid angle of the radiation illuminating the satellite at 500 km altitude.

3.2 Galactic Emission

The Galactic gamma emission[108,109] which consists of diffuse continuum[110] and resolved sources has been widely observed by many instruments, e.g. by *SAS-2*,[77,111–113] *OSO-3*,[114] *COS B*,[113,115]

13

INTEGRAL[82,87,116–120] satellites, COMPTEL, EGRET and OSSE instruments[81,121–124] aboard the *CGRO* satellite, *Fermi*/LAT,[88,125–127] *RXTE*/PCA[128] and *Swift*/BAT[129] instruments.

For our MC simulations (Sec. 7) we took the X-ray/gamma-ray fluxes of the inner Galactic region from Figures 10 and 11 as published in Ref. 87 in EF_E flux density representation. Ref. 87 summarizes measurements from *RXTE*/PCA,[116] *INTEGRAL*/SPI,[118] *INTEGRAL*/IBIS,[87,116] *CGRO*/COMPTEL[117] and *CGRO*/EGRET[117] instruments and show the fluxes renormalized to the central radian of the Milky Way defined by $|l| < 30°$ and $|b| < 15°$.

The emission from the inner Galactic region irradiates a satellite from the solid angle of $0.542\,$sr. The differential and integral photon spectra are shown in Figure 5. The integral flux for energy $E > 10\,$keV is $0.2\,$ph cm^{-2}s^{-1}. However, it should be noted that the Galactic emission is not spatially uniform and has a brightness structure peaked at the Galactic center (see e.g. Ref. 115). Figure 5 also shows measurements done by *Fermi*/LAT taken from Figure 4 of Ref. 125 for smaller region of $|l| < 30°$ and $|b| < 10°$. We do not include these *Fermi*/LAT measurements in our MC simulations because the region of the inner Galaxy is not exactly the same as the one used for the other aforementioned data sets. This does not effect our results because the photon flux at these very high energies is very small.

3.3 Trapped Particles

The fluxes of the geomagnetically trapped electrons and protons inside the inner van Allen radiation belt[130] contribute to the overall detected instrumental background and they are especially important when a satellite at LEO passes the polar regions[131,132] or the South Atlantic Anomaly (SAA). Details about the Earth's radiation environment can be found in, for example, Ref. 58,64, 133–139.
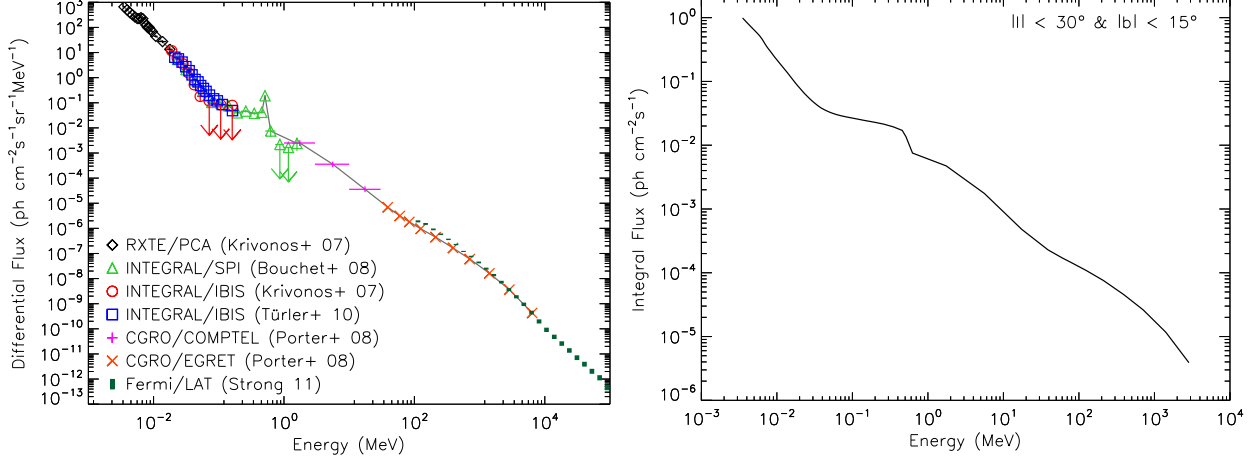
Fig 5 The spectra of the inner Galaxy emission. *Left:* The differential photon flux observed by *RXTE*/PCA,[116] *INTE-GRAL*/SPI,[118] *INTEGRAL*/IBIS,[87,116] *CGRO*/COMPTEL[117] and *CGRO*/EGRET[117] for the region defined by $|l| < 30°$, $|b| < 15°$ and *Fermi*/LAT[125] for the region defined by $|l| < 30°$, $|b| < 10°$. The gray solid line marks the flux taken for our MC simulations. *Right:* The integral photon flux. The integral flux is multiplied by 0.542 sr solid angle of the inner Galaxy region.

Several models describing the fluxes of the trapped particles around the Earth based on measurements from tens of space missions have been developed over last decades, e.g. the National Aeronautics and Space Administration's (NASA) AE8[140,141] and AP8[141,142] models, European Space Agency's (ESA) AE-8 update ESA-SEE1[143] model, or model based on the measurements from Proton/Electron Telescope (PET) onboard the Solar, Anomalous, and Magnetospheric Particle Explorer (*SAMPEX*) satellite - the *SAMPEX*/PET PSB97 model.[144]

In our on-board background simulations (Sec. 7) we employ the fluxes of trapped electrons and protons prescribed by the recent AE9 and AP9 models[145–148] as they are implemented in ESA's SPace ENVironment Information System (SPENVIS[5]). SPENVIS is an Internet interface to models of the space environment and its effects, developed by a consortium led by the Royal Belgian Institute for Space Aeronomy (BIRA-IASB). The AE9/AP9 models are based on 33 satellite data sets from 1976 to 2011 and they are provided by the U.S. Air Force Research Laboratory (AFRL)

---

[5]www.spenvis.oma.be

in their software package [6].

The AE8/AP8 models available in SPENVIS or in the AFRL package do not compute fluxes lower than 1 particle $\mathrm{cm^{-2}s^{-1}}$, whereas the AE9/AP9 models provide fluxes below 1 particle $\mathrm{cm^{-2}s^{-1}}$. That is important for our purpose, because we want to estimate the detected background count rate in the regions outside SAA and polar regions. However, the current version of the AP9/AE9 model provided in SPENVIS is recommended for evaluation purposes only and there have been reported discrepancies between the AE8/AP8 and the AE9/AP9 models, e.g. see Ref. 149 and references therein.

Figure 6 shows orbit-averaged integral spectra of trapped electrons and protons averaged over 60 days of orbiting (including SAA passages) with sampling of 10 s obtained for different models by the AFRL package. It demonstrates that AE9/AP9 models gives much higher electron and proton fluxes compared to the AE8/AP8 models at low inclinations and low energies. Therefore the detected background count rate due to the trapped particles calculated by our simulation may overestimate the real level.

Figure 7 shows maps of integral fluxes (flux of particles with energy higher than E) of trapped electrons and protons for the AE9 and AP9 models with Monte Carlo (MC) mode, 100 runs and 50 % confidence level (CL) at 500 km altitude. The MC mode accounts for the uncertainty due to the random perturbations as well as the flux variations due to the space weather.[145]

We calculated spectra of electrons and protons averaged along the trajectory of a satellite at altitude 500 km with inclination of $i = 20°$ and orbiting 30 days with flux sampling every 10 s. Only the regions with the integral flux ≤ 10 particle $\mathrm{cm^{-2}s^{-1}}$ were used ($E > 40\,\mathrm{keV}$ for electrons and $E > 100\,\mathrm{keV}$ for protons). These conditions give a duty cycle, i.e. the fraction of time a

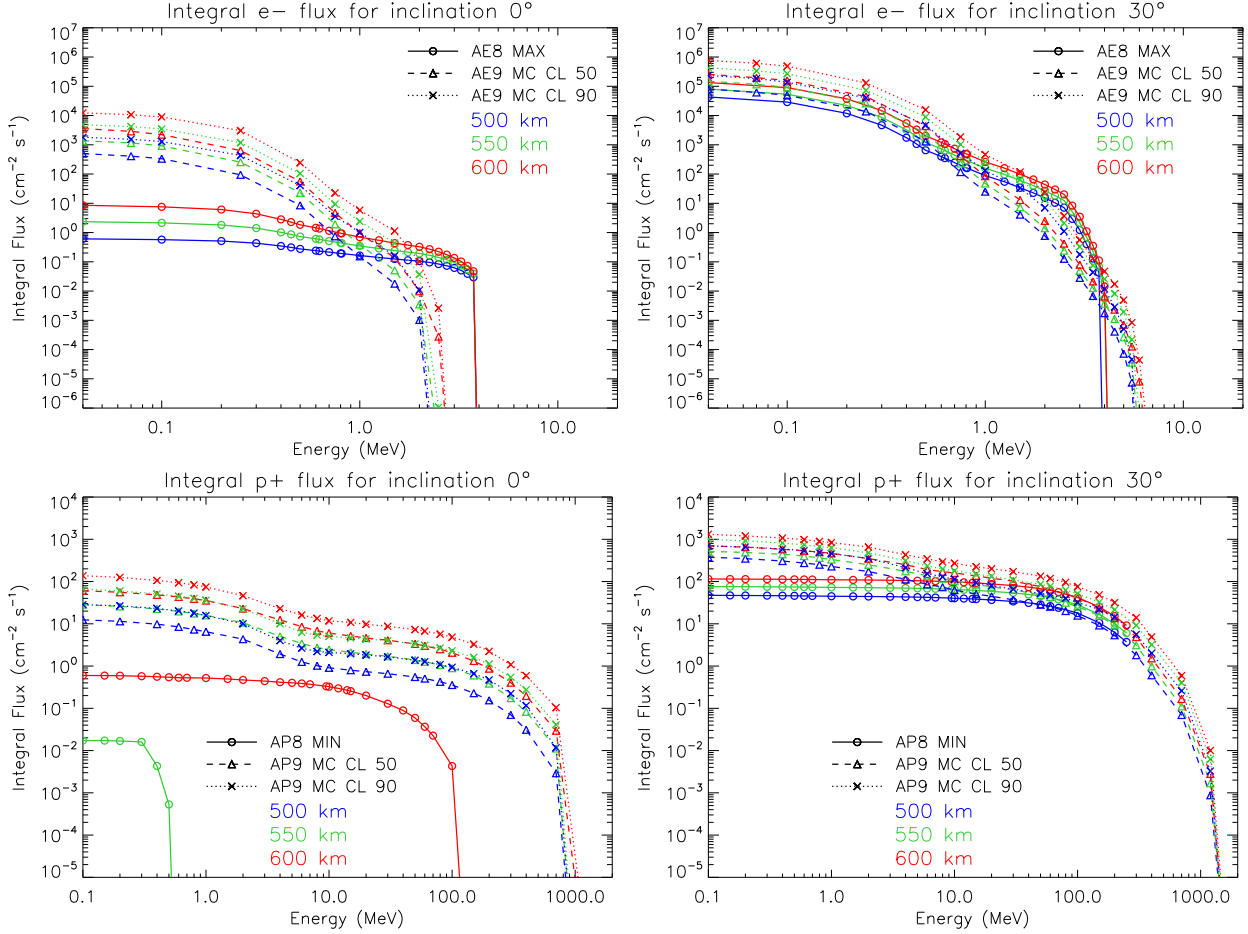---

[6]https://www.vdl.afrl.af.mil/programs/ae9ap9

Fig 6 Comparison of orbit-averaged integral fluxes of trapped electron models AE8 MAX (solar maximum), AE9 50 % and 90 % confidence levels (CL); and trapped proton models AP8 MIN (solar minimum), AP9 50 % and 90 % CL for different altitudes and inclinations.

satellite spends in a region with particle flux lower than a given flux threshold, of 80 %. If the orbital inclination is 90° the duty cycle would be 76 %. Details about the duty cycle for different inclinations, altitudes at LEO, flux and energy thresholds for AE8, AP8, AE9 and AP9 models can be found in Ref. 150.

In this way we were able to obtain averaged spectra outside of SAA. The differential and integral fluxes are shown in Figure 8. The differential flux per solid angle has been calculated for simplicity assuming the radiation is illuminating a satellite isotropically from the solid angle of 4π because, for example, in case of *CAMELOT* satellites the pointing strategy is not established yet.
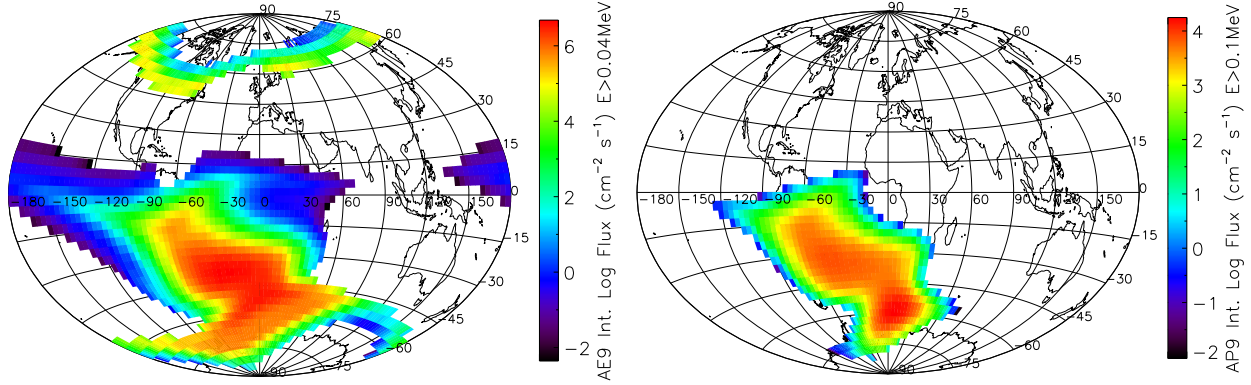
Fig 7 A map of the integral flux of geomagnetically trapped electrons (left) and protons (right) at 500 km altitude according to the AE9 and AP9 models (MC mode, 50 % CL), respectively, obtained by the AFRL package.

The trapped particles can collide with the detector from various directions and we are interested in a long-term average. Also, the assumption of the isotropy of the trapped particle flux is a simplification because of the well known "East-West" effect.[151] The integral flux for trapped electrons is $0.41\,\mathrm{cm}^{-2}\mathrm{s}^{-1}$ ($E > 40\,\mathrm{keV}$) and for trapped protons is $0.14\,\mathrm{cm}^{-2}\mathrm{s}^{-1}$ ($E > 100\,\mathrm{keV}$) as obtained from the model.
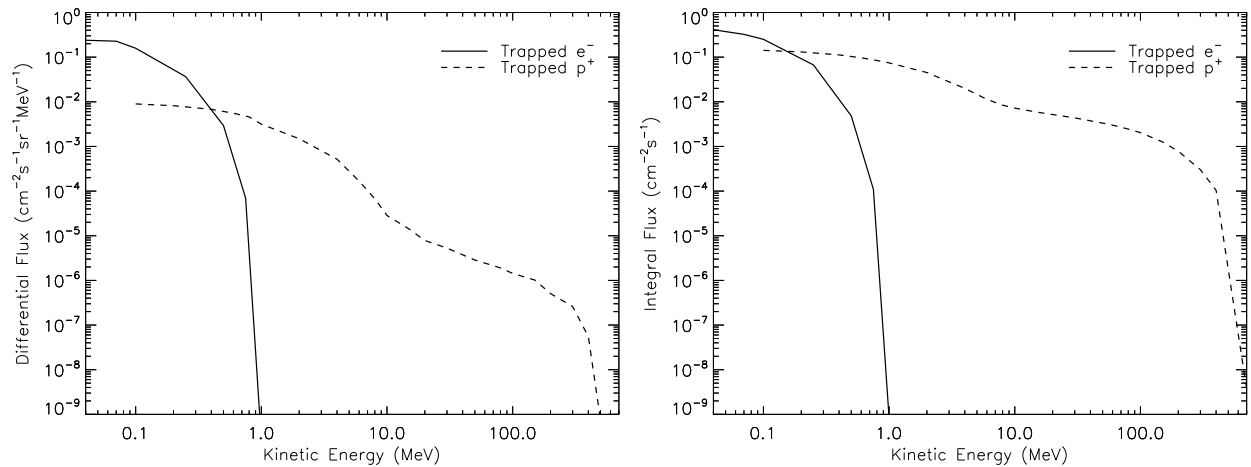

Fig 8 Differential fluxes (left) and integral fluxes (right) of geomagnetically trapped electrons and protons averaged along the trajectory of a satellite at altitude 500 km with inclination $i = 20°$ and orbiting 30 days. The models were AE9 and AP9, MC mode with 100 runs and the spectra were derived from the 50 % CL of the fluxes. Only the regions avoiding SAA were used. The differential flux per solid angle has been calculated for simplicity assuming the radiation is illuminating the satellite isotropically from the solid angle of 4π.

18

3.4 Primary Cosmic-Rays

The spectra of the primary particles of cosmic-rays (CRs) used in our simulations are described below. For the assumed 500 km altitude the fluxes irradiate the satellite from the solid angle of 8.64 sr. The origin of CRs is extraterrestrial consisting mainly of protons. Other components of CRs such as electrons, positrons, alpha particles and nuclei of heavier elements have been detected as well. Several experiments have been performed to study CRs, e.g. AMS,[152,153] BESS,[154] CREAM,[155] *Fermi*/LAT,[156,157] HESS,[158] PAMELA.[159]

We considered two models for the spectra of primary particles. The first one was the ISO-15390[160] model, which is the international standard for estimating the radiation impact of CRs on hardware in space and which describes the fluxes of primary protons, alpha particles, and nuclei of heavier elements.

The second model which we considered was described by Mizuno et al. (2004), see Ref. 63, and it was based on measurements done by BESS and AMS experiments (see also Ref. 66). The flux of primary CRs in interstellar space can be modeled by a power law function:

$$F_{\mathrm{U}}(E_{\mathrm{k}}) = A \left[\frac{R(E_{\mathrm{k}})}{\mathrm{GV}} \right]^{-a}, \tag{6}$$

where $R = pc/Ze$ is the rigidity of the particle as a function of its kinetic energy E_{k} or momentum p and its charge Ze. The flux constant A and the exponent a are determined by fitting of the following model to the measurements.

The flux of primary CRs for a given phase of the solar cycle and in a given position in the

Earth's magnetosphere according to the model described in Ref. [63] is:

$$F(E_k) = F_U(E_k + Ze\phi) \times F_M(E_k, M, Z, \phi) \times F_C(R, h, \theta_M), \tag{7}$$

where M is the mass of the particle, ϕ is a solar modulation potential, h is the altitude of the satellite's orbit and θ_M is the geomagnetic latitude.

By applying an effective shift of energy of the primary particles due to the deceleration by the solar wind the first function F_U in Eq. (7) gets form:

$$F_U(E_k + Ze\phi) = A \left[\frac{R(E_k + Ze\phi)}{\text{GV}} \right]^{-a}. \tag{8}$$

The second function F_M accounts for the flux modulation due to the solar cycle and is given by:

$$F_M(E_k, M, Z, \phi) = \frac{(E_k + Mc^2)^2 - (Mc^2)^2}{(E_k + Ze\phi + Mc^2)^2 - (Mc^2)^2}, \tag{9}$$

where the solar modulation potential varies between $\phi = 0.55\,\text{GV}$ for solar minimum and $\phi = 1.10\,\text{GV}$ for solar maximum.

The third term is the geomagnetic cutoff function F_C given by:

$$F_C(R, h, \theta_M) = \frac{1}{1 + (R/R_{\text{cut}})^{-r}}, \tag{10}$$

where $r = 12$ for p^+ or α particles, $r = 6$ for e^- or e^+, and the cutoff rigidity R_{cut} is given by the Störmer equation:[161]

$$R_{\text{cut}} = 14.5 \left(1 + \frac{h}{R_E} \right)^{-2} \cos^4 \theta_M \, \text{GV}, \tag{11}$$

where R_E is the Earth's radius.

We want to estimate a long term average of the flux, therefore we assume that the flux has uniform angular distribution for the zenith angle $0° \leq \theta \leq \theta_\mathrm{cut}$ and the flux is zero for $\theta_\mathrm{cut} \leq \theta \leq 180°$, where the θ_cut is the zenith angle of the Earth's horizon and it is $112°$ for the altitude of $500\,\mathrm{km}$.

3.4.1 Primary Protons and Alpha Particles

For primary protons and alpha particles we compared the model ISO-15390 and the model Mizuno et al. (2004) described in Ref. 63.

For the ISO-15390 model we employed SPENVIS where we generated the orbit-averaged spectra for circular orbit with inclination $i = 20°$, duration 30 days and sampling $60\,\mathrm{s}$. The following parameters setting was applied: solar minimum activity (May 1996), magnetic shielding on, stormy and quite magnetosphere, Størmer with eccentric dipole method and magnetic field moment unchanged.

For the model described in Ref. 63 we used the following parameters: solar minimum cycle with the solar modulation potential $\phi = 0.55\,\mathrm{GV}$, altitude $500\,\mathrm{km}$, and two geomagnetic latitudes $\theta_\mathrm{M} = 0°$ and $\theta_\mathrm{M} = 20°$ (orbital inclination) $+ 9.6°$ (tilt between the geomagnetic dipole axis and the Earth's rotational axis).

For primary protons the values of $A = 23.9\,\mathrm{particle\,m^{-2}s^{-1}sr^{-1}MeV^{-1}}$ and $a = 2.83$ were adopted. For primary alpha particles the values of $A = 1.5\,\mathrm{particle\,m^{-2}s^{-1}sr^{-1}MeV^{-1}}$ and $a = 2.77$ were adopted.

Figure 9 and 10 show fluxes of primary protons and alpha particles, respectively, at $500\,\mathrm{km}$ altitude obtained by the ISO-15390 model for quiet and stormy magnetosphere and obtained by the

Mizuno et al. (2004) model for fixed geomagnetic latitudes $\theta_M = 0°$ and $\theta_M = 29.6°$. This model predicts the integral flux of primary protons of kinetic energies $E > 1\,\text{GeV}$ being $0.11\,\text{cm}^{-2}\text{s}^{-1}$ (for $\theta_M = 0°$) or $0.29\,\text{cm}^{-2}\text{s}^{-1}$ (for $\theta_M = 29.6°$) and the integral flux of primary alpha particles of kinetic energies per nucleon $E > 1\,\text{GeV/n}$ being $0.016\,\text{cm}^{-2}\text{s}^{-1}$ (for $\theta_M = 0°$) or $0.041\,\text{cm}^{-2}\text{s}^{-1}$ ($\theta_M = 29.6°$).

For our Geant4 simulations of the expected on-board background by a *CAMELOT* satellite (Sec. 7) we use the ISO-15390 model with stormy magnetosphere, because it is the international standard for CR flux and because it was obtained for a fixed orbital inclination of $i = 20°$ meaning crossing the range of geomagnetic latitudes between $-30°$ and $\sim 32°$[7],[162] It predicts the integral flux of primary protons of kinetic energies $E > 1\,\text{GeV}$ being $0.095\,\text{cm}^{-2}\text{s}^{-1}$ (for quite magnetosphere) or $0.099\,\text{cm}^{-2}\text{s}^{-1}$ (for stormy magnetosphere) and the integral flux of primary alpha particles of kinetic energies per nucleon $E > 1\,\text{GeV/n}$ being $0.017\,\text{cm}^{-2}\text{s}^{-1}$ (for quite magnetosphere) or $0.018\,\text{cm}^{-2}\text{s}^{-1}$ (for stormy magnetosphere).

3.4.2 Primary Electrons and Positrons

For the spectra of the primary e^- and e^+ we used the model described by Mizuno et al. (2004)[63] with references to the flux measurements by.[163,164] The measurements of the ratio of positrons and electrons $e^+/(e^-+e^+)$ are given by.[153,165]

We adopt the model of the primary interstellar particles Eq. (6) with following parameters: $A = 0.65\,\text{particle}\,\text{m}^{-2}\text{s}^{-1}\text{sr}^{-1}\text{MeV}^{-1}$ and $a = 3.3$ for electrons and $A = 0.051\,\text{particle}\,\text{m}^{-2}\text{s}^{-1}\text{sr}^{-1}\text{MeV}^{-1}$ with the same exponent a for positrons.

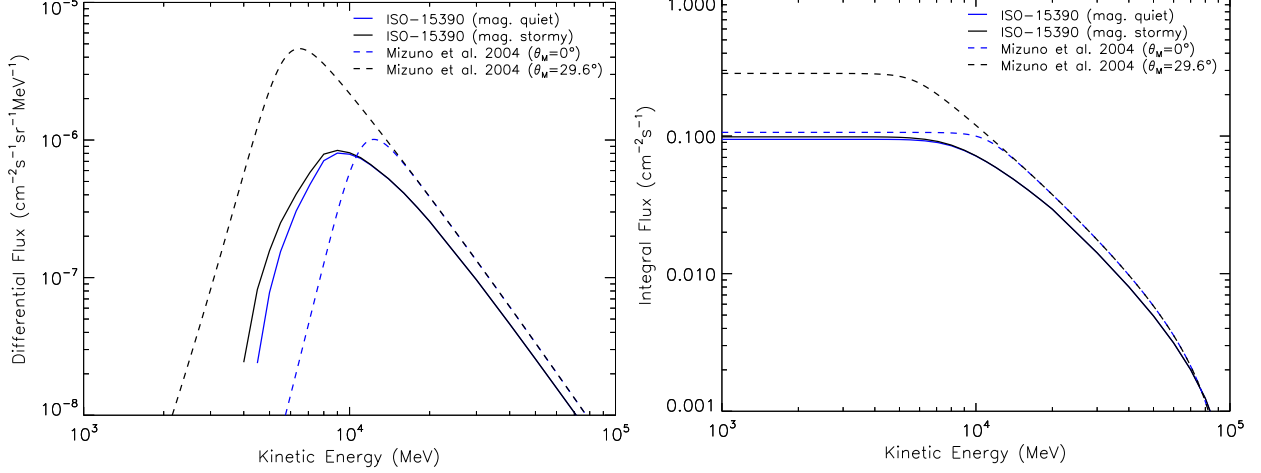Same as for the primary protons and alpha particles we used the following conditions of the

---

[7]https://spawx.nwra.com/spawx/maps/maplats.html

Fig 9 Differential fluxes (left) and integral fluxes (right) of primary CR protons. Solid lines mark model introduced by Mizuno et al. (2004)[63] for geomagnetic latitudes $\theta_{\mathrm{M}} = 0°$ and $\theta_{\mathrm{M}} = 29.6°$. Dashed lines mark galactic CR model ISO-15390[160] for quiet and stormy magnetosphere obtained in SPENVIS for circular orbit with inclination $i = 20°$. Spectra from both models were obtained for altitude of 500 km. The integral flux is multiplied by a solid angle corresponding to the radiation illuminating the satellite at this altitude.
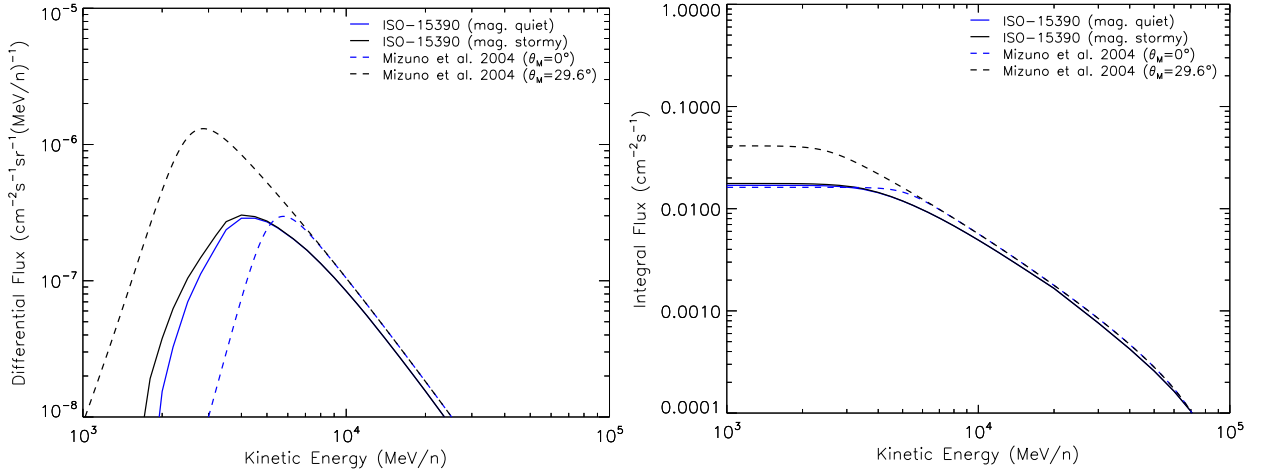

Fig 10 Differential fluxes (left) and integral fluxes (right) of primary CR alpha particles as a function of energy per nucleon. Solid lines mark model introduced by Mizuno et al. (2004)[63] for geomagnetic latitudes $\theta_{\mathrm{M}} = 0°$ and $\theta_{\mathrm{M}} = 29.6°$. Dashed lines mark galactic CR model ISO-15390[160] for quiet and stormy magnetosphere obtained in SPENVIS for circular orbit with inclination $i = 20°$. Spectra from both models were obtained for altitude of 500 km. The integral flux is multiplied by a solid angle corresponding to the radiation illuminating the satellite at this altitude.

solar cycle and the orbit: solar minimum with the modulation potential $\phi = 0.55\,\mathrm{GV}$, altitude 500 km, and two geomagnetic latitudes $\theta_{\mathrm{M}} = 0°$ and $\theta_{\mathrm{M}} = 29.6°$. Figure 11 and 12 show the fluxes of the primary electrons and positrons.

For our simulations of the expected detected background (Sec. 7) we use the spectrum for

23

$\theta_M = 29.6°$. We also assume that the angular distribution of the flux is incoming uniformly from the solid angle unocculted by the Earth. Then the integral flux ($E > 1\,\mathrm{GeV}$) for e⁻ is $3 \times 10^{-3}\,\mathrm{cm^{-2}s^{-1}}$ and for e⁺ it is $2.3 \times 10^{-4}\,\mathrm{cm^{-2}s^{-1}}$.
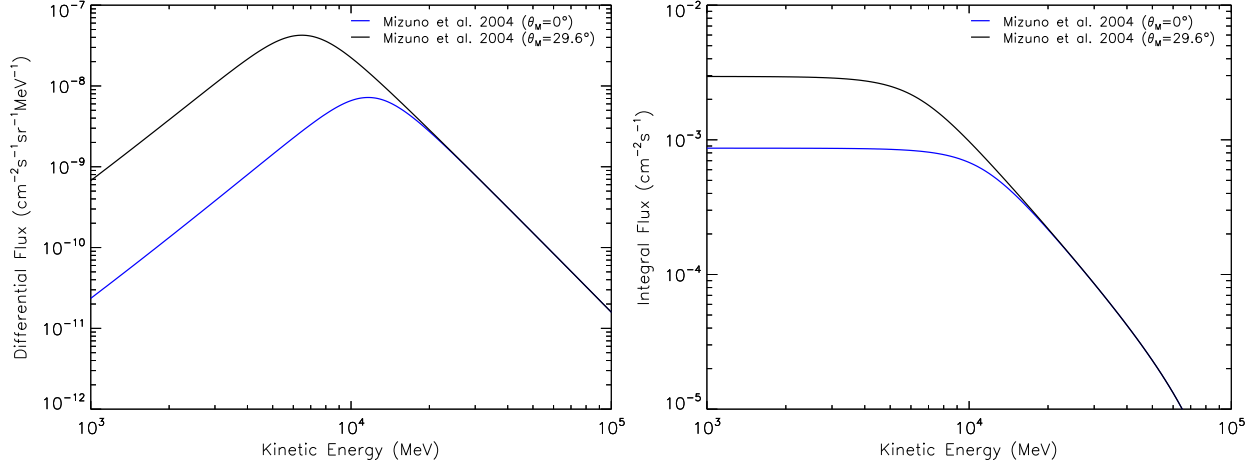

Fig 11 Differential fluxes (left) and integral fluxes (right) of primary CR electrons modeled by Mizuno et al. (2004)[63] for geomagnetic latitudes $\theta_M = 0°$ and $\theta_M = 29.6°$ and altitude of 500 km. The integral flux is multiplied by a solid angle corresponding to the radiation illuminating the satellite at this altitude.

Fig 12 Differential fluxes (left) and integral fluxes (right) of primary CR positrons modeled by Mizuno et al. (2004)[63] for geomagnetic latitudes $\theta_M = 0°$ and $\theta_M = 29.6°$ and altitude of 500 km. The integral flux is multiplied by a solid angle corresponding to the radiation illuminating the satellite at this altitude.
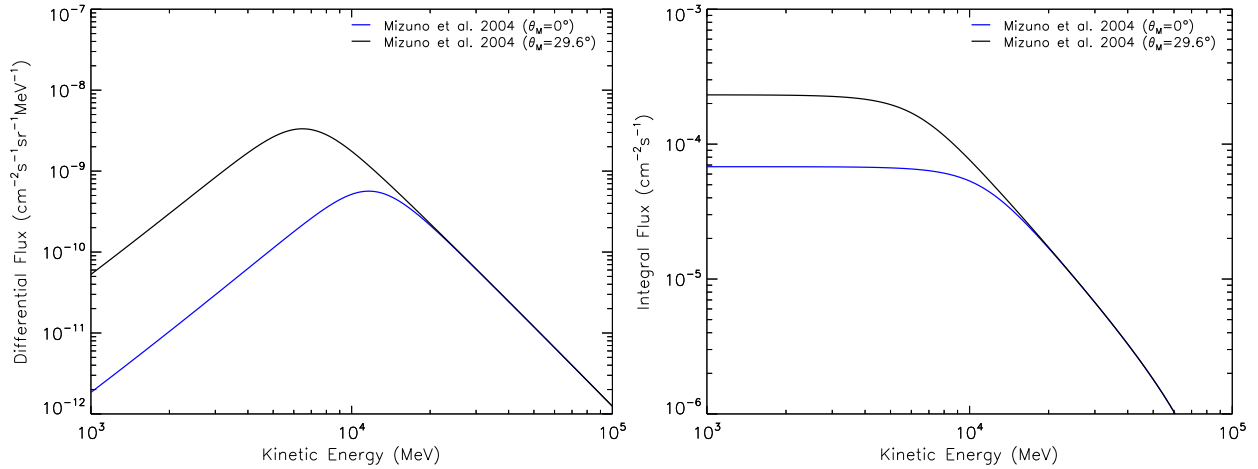
3.5 Secondary Particles and Radiation

Secondary (albedo) particles and radiation are created by interaction of primary CRs with the Earth's atmosphere.[58,64]

3.5.1 Secondary Protons

For secondary p^+ and for energy above 100 MeV we use the model[63] based on the measurements done by the Alpha Magnetic Spectrometer (AMS)[152] from 380 km altitude for the geomagnetic latitude 0.3 rad $\leq \theta_M \leq 0.4$ rad. For energy below 100 MeV we use the fit to *MITA*/NINA-2 data[166] from 450 km altitude and for $1.0 \leq$ L-shell ≤ 1.7, where L-shell is the McIlwain L-parameter.[167] For details see the LAT Technical Note LAT-TD-08316-01[72] of the *Fermi* satellite.[168] There is only small dependence of the flux on altitude[166,169] therefore it can be used as an approximation to the flux at altitude of 500 km.

The differential flux $F(E)$ in units of particle $\mathrm{m}^{-2}\mathrm{s}^{-1}\mathrm{sr}^{-1}\mathrm{MeV}^{-1}$ is modeled as:

$$F(E) = \begin{cases} 0.1 \left(\frac{E}{100\,\mathrm{MeV}}\right)^{0.4} & \text{for } 10\,\mathrm{MeV} \leq E \leq 100\,\mathrm{MeV} \\ 0.1 \left(\frac{E}{100\,\mathrm{MeV}}\right)^{-1.09} & \text{for } 100\,\mathrm{MeV} \leq E \leq E_{\mathrm{brk}} \\ 0.1 \left(\frac{E_{\mathrm{brk}}}{100\,\mathrm{MeV}}\right)^{-1.09} \left(\frac{E}{E_{\mathrm{brk}}}\right)^{-2.4} & \text{for } E \geq E_{\mathrm{brk}}, \end{cases} \tag{12}$$

where $E_{\mathrm{brk}} = 600$ MeV is break energy. Figure 13 shows the modeled flux together with the measurements.

The same model is used for the upward and downward component of the flux and it is assumed that secondary protons irradiate the satellite from the solid angle of 4π sr without zenith-angle dependence of the flux. The integral flux ($E \geq 10$ MeV) is $0.037\,\mathrm{cm}^{-2}\mathrm{s}^{-1}$.
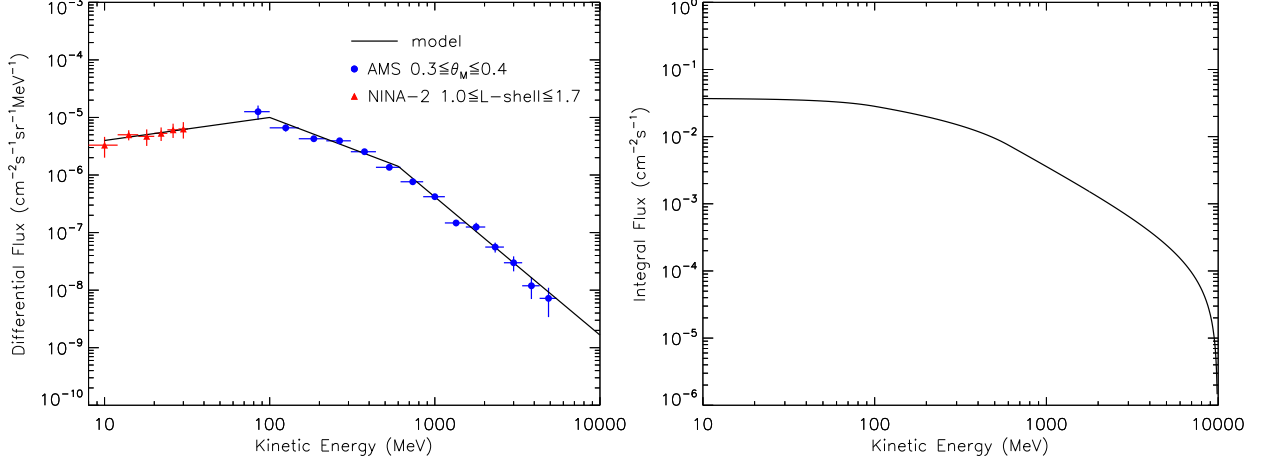
Fig 13 Differential fluxes (left) and integral fluxes (right) of secondary protons modeled by Eq. (12) are marked by the black curve. The measurements from the AMS and *MITA*/NINA-2 experiments for the given geomagnetic position are shown as well. The integral flux is multiplied by the solid angle of 4π sr.

3.5.2 Secondary Electrons and Positrons

For secondary e$^-$ and e$^+$ and for energy above $100\,\mathrm{MeV}$ we use the model[63] based on the measurements done by AMS[152] from $380\,\mathrm{km}$ altitude for the geomagnetic latitude $0 \leq \theta_\mathrm{M} \leq 0.3$ rad. For energy below $100\,\mathrm{MeV}$ we use the fit to *Mir*/MARIA-2 data[170,171] from $400\,\mathrm{km}$ altitude and for $1.0 \leq$ L-shell ≤ 1.2. For details see the LAT Technical Note LAT-TD-08316-01.[72]

For secondary e$^-$ the differential flux $F(E)$ in units of particle $\mathrm{m^{-2}s^{-1}sr^{-1}MeV^{-1}}$ is modeled as:

$$F(E) = \begin{cases} 0.3 \left(\frac{E}{100\,\mathrm{MeV}}\right)^{-2.0} & \text{for } 10\,\mathrm{MeV} \leq E \leq 100\,\mathrm{MeV} \\[2ex] 0.3 \left(\frac{E}{100\,\mathrm{MeV}}\right)^{-2.2} & \text{for } 100\,\mathrm{MeV} \leq E \leq E_\mathrm{brk} \\[2ex] 0.3 \left(\frac{E_\mathrm{brk}}{100\,\mathrm{MeV}}\right)^{-2.2} \left(\frac{E}{E_\mathrm{brk}}\right)^{-4.0} & \text{for } E \geq E_\mathrm{brk}, \end{cases} \tag{13}$$

where the break energy $E_\mathrm{brk} = 3000\,\mathrm{MeV}$. Figure 14 shows the modeled flux together with the measurements.

For secondary e$^+$ the differential flux $F(E)$ in units of particle $\mathrm{m^{-2}s^{-1}sr^{-1}MeV^{-1}}$ is modeled
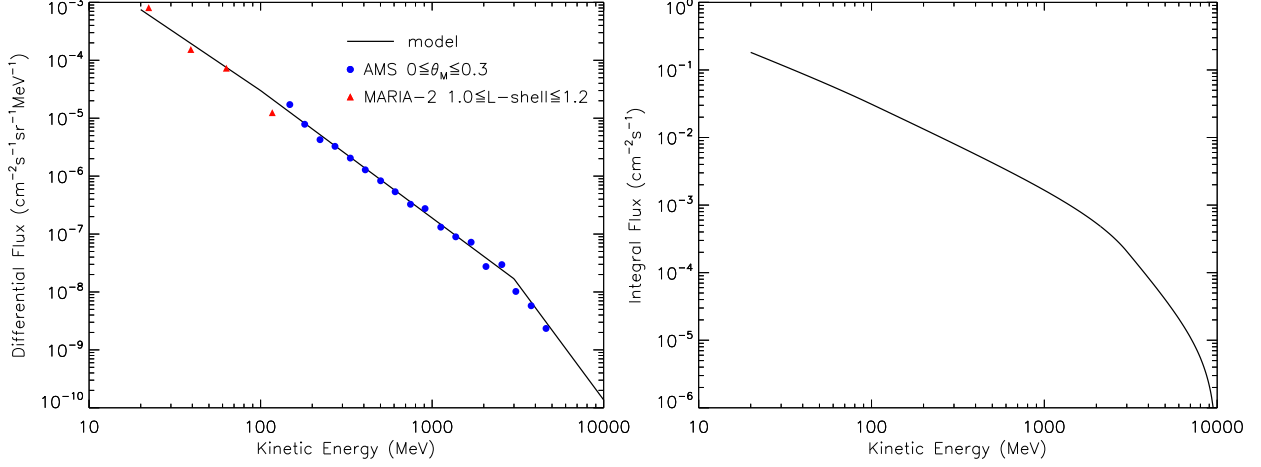
Fig 14 Differential fluxes (left) and integral fluxes (right) of secondary electrons modeled by Eq. (13) are marked by the black curve. The measurements from the AMS and *Mir*/MARIA-2 experiments for the given geomagnetic position are shown as well. The integral flux is multiplied by the solid angle of 4π sr.

as:

$$
F(E) = \begin{cases}
20 \left(\frac{E}{10\,\text{MeV}}\right)^{-1.77} & \text{for } 10\,\text{MeV} \leq E \leq 60\,\text{MeV} \\[2mm]
0.833 \left(\frac{E}{60\,\text{MeV}}\right)^{-1.0} & \text{for } 60\,\text{MeV} \leq E \leq 178\,\text{MeV} \\[2mm]
1.0 \left(\frac{E}{100\,\text{MeV}}\right)^{-2.2} & \text{for } 178\,\text{MeV} \leq E \leq E_{\text{brk}} \\[2mm]
1.0 \left(\frac{E_{\text{brk}}}{100\,\text{MeV}}\right)^{-2.2} \left(\frac{E}{E_{\text{brk}}}\right)^{-4.0} & \text{for } E \geq E_{\text{brk}},
\end{cases}
\tag{14}
$$

where the break energy $E_{\text{brk}} = 3000\,\text{MeV}$. Figure 15 shows the modeled flux together with the measurements.

The same model is used for the upward and downward component of the flux and it is assumed that secondary e^- and e^+ irradiate the satellite from the solid angle of 4π sr without zenith-angle dependence of the flux. The integral flux ($E \geq 20\,\text{MeV}$) is $0.18\,\text{cm}^{-2}\text{s}^{-1}$ for e^- and $0.23\,\text{cm}^{-2}\text{s}^{-1}$ for e^+.
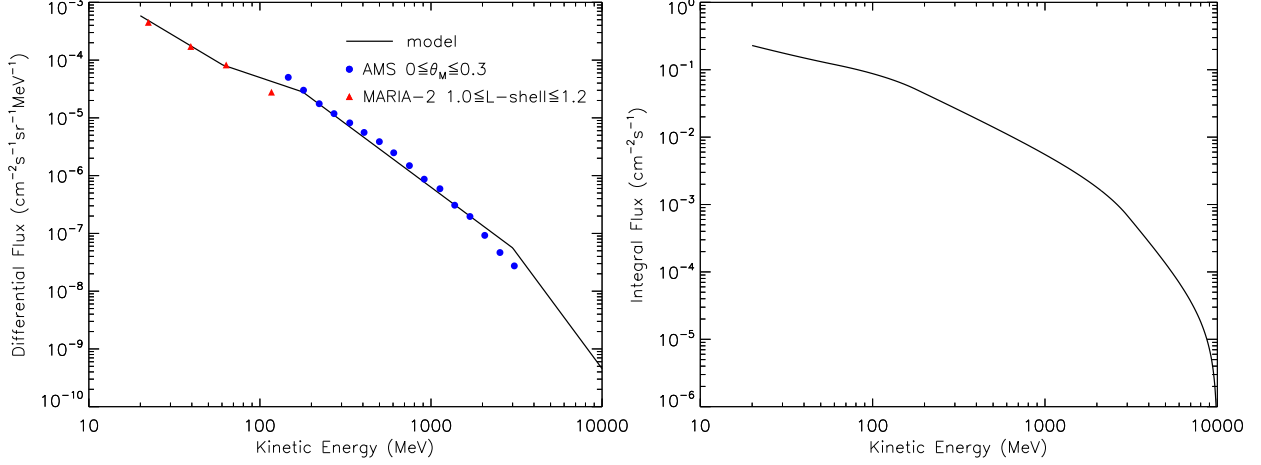
27

Fig 15 Differential fluxes (left) and integral fluxes (right) of secondary positrons modeled by Eq. (14) are marked by the black curve. The measurements from the AMS and *Mir*/MARIA-2 experiments for the given geomagnetic position are shown as well. The integral flux is multiplied by the solid angle of 4π sr.

3.5.3 *Albedo X-rays/γ-rays*

The secondary (albedo) X-ray and γ-ray flux is due to interaction of primary CRs with the Earth's atmosphere. It is produced by decay of π^0 pions (mainly above 50 MeV), by bremsstrahlung from primary and secondary electrons (mainly below 50 MeV), and also by the reflection of CXB and it has been measured by several satellites and balloon experiments.[60,61,63,64,69,75,76,78,82,87,172–177] The intensity depends on the geomagnetic latitude.[178]

We utilize a model reported by Ajello et al. (2008)[84] based on the *Swift*/BAT measurements from ~ 20 keV to ~ 200 keV for altitude of $h \sim 550$ km and inclination of $i = 20.6°$ and which is compatible with measurements from BeppoSAX[83] ($h \sim 580$ km and $i = 4°$) and after some corrections with measurements by the polar-orbiting satellite 1972-076B[178] ($h \sim 750$ km). MC simulations show that this model is a very good approximation of the Earth albedo X-ray emission up to 300 keV.[84,179]

We assume the Ajello et al. (2008) model[84] in the energy range of $E = 10 - 300$ keV and hence the differential photon flux $F(E)$ given by Eq. (5), where the model parameters and their

90 % CL errors are Γ_1=-5 (fixed), Γ_2=1.72±0.08, E_b=33.7±3.5 keV and $C = 1.48^{+0.6}_{-0.3} \times 10^{-2}$.

For higher energies we assume a model reported by Mizuno et al. (2004)[63] based on measurements by *1972-076B* and *Kosmos 461* satellites[173,178] and by balloon flights.[172,174] Particularly, we consider only energies $E = 0.3 - 20$ MeV where we assume the differential photon flux $F(E)$ in units of $\mathrm{ph\,cm^{-2}s^{-1}sr^{-1}keV^{-1}}$ to be a simple power law function:

$$F(E) = 719 \left(\frac{E}{\mathrm{keV}} \right)^{-1.34}, \tag{15}$$

where we normalized the Mizuno et al. (2004) model,[63] their Eq. (21), in order to obtain the same differential flux at 300 keV as predicted by the Ajello et al. (2008) model.[84] The spectrum is shown in Figure 16. According to MC simulations[179] there is only a small dependence of the albedo X-ray flux (25 − 300 keV) on the solar cycle and geomagnetic latitude below $\sim 20°$ for an instrument at LEO with large FOV which covers the whole terrestrial disc.
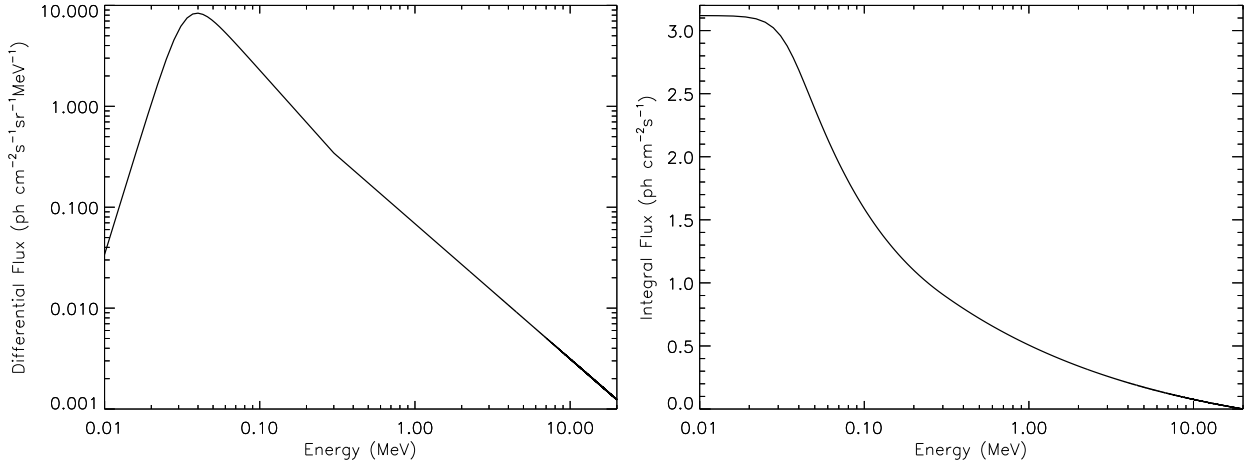

Fig 16 The albedo X-ray/γ-ray spectra. For energies from 10 keV to 300 keV modeled by Ajello et al. (2008) and for energies from 300 keV to 20 MeV modeled by Eq. (15). *Left:* The differential photon flux. *Right:* The integral photon flux integrated up to 20 MeV. The integral flux is multiplied by the Earth-subtended solid angle of 3.93 sr at an altitude of 500 km.

A zenith angle dependence of the albedo γ-ray flux has been measured in the $1 - 10$ MeV

region.[63,75,76] See also Ref. [61,114,172,174–178,180] and references therein for the zenith angle dependence of the albedo γ-ray flux at other energies. In the energy range $25 - 300\,\text{keV}$, covered by the Ajello et al. (2008) model, the MC simulations[179] suggest that there is no zenith angle dependence. However, for the higher-energy part $0.3 - 20\,\text{MeV}$ one can expect a zenith angle dependence of the flux. In case of *CAMELOT* satellites, they will have detectors with all-sky FOV which can be illuminated from various directions and we are interested in a long term average flux, therefore, for simplicity, we do not assume any zenith angle dependence in our Geant4 simulations involving a *CAMELOT* satellite mass model.

At an altitude of $500\,\text{km}$ the photons would irradiate the satellite from a solid angle of $3.93\,\text{sr}$. The integral flux ($E > 10\,\text{keV}$) is $3.1\,\text{ph}\,\text{cm}^{-2}\text{s}^{-1}$.

3.5.4 Albedo Neutrons

The albedo neutrons are produced in hadronic showers created by CRs interacting with the Earth's atmosphere and they can reach a satellite at LEO.[69] For the albedo neutrons we use the predictions of the QinetiQ Atmospheric Radiation Model (QARM), based on MC radiation transport code, as reported in the ESA document ECSS-E-ST-10-04C.[71] The model has been validated against several measurements[181–184] and is also consistent with other MC simulations.[59,65] For other models and measurements see Ref. [61,69,185,186] and references therein.

Figure 17 shows the fluxes of secondary neutrons for the cutoff rigidity $R_{\text{cut}} = 16.6\,\text{GV}$ and $R_{\text{cut}} = 5\,\text{GV}$ for solar minimum. The fluxes were scaled from the altitude of $100\,\text{km}$ to $500\,\text{km}$ as described in the ECSS-E-ST-10-04C document.

In our simulations of the expected detected background (Sec. 7) we use the spectrum for the solar minimum and for the cutoff rigidity $R_{\text{cut}} = 5\,\text{GV}$ which corresponds to the geomagnetic

latitude $\theta_{\mathrm{M}} = 37°$ following from the Störmer equation Eq. (11) or latitude between $\sim 30°$ and $\sim 50°$, see Figure 7 of Ref. 161.

The integral flux is $0.61\,\mathrm{cm}^{-2}\mathrm{s}^{-1}$ for $E > 1\,\mathrm{eV}$, for $R_{\mathrm{cut}} = 5\,\mathrm{GV}$, altitude of $500\,\mathrm{km}$ and assuming that all neutrons are coming from the solid angle of $3.93\,\mathrm{sr}$ which corresponds to the angular size of the Earth observed from that altitude.
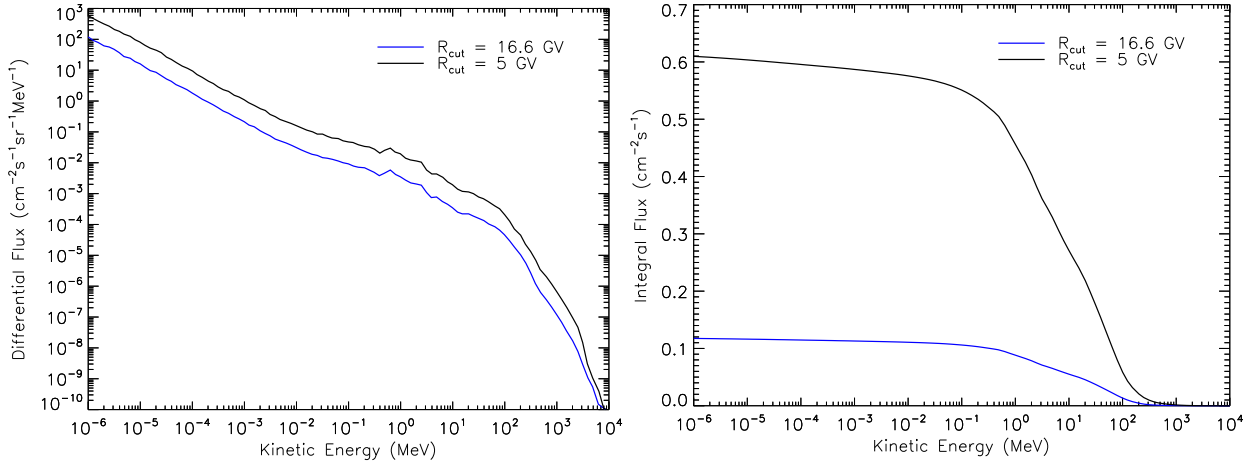

Fig 17 Differential fluxes (left) and integral fluxes (right) of albedo neutrons predicted by the QARM model for two values of cutoff rigidity and scaled to the altitude of $500\,\mathrm{km}$. The integral flux is multiplied by the solid angle of $3.93\,\mathrm{sr}$.

4 The *CAMELOT* CubeSats

We study in particular the expected on-board background for the proposed *CAMELOT* mission, expected to be launched to LEO with the main objective of all-sky monitoring and timing-based localization of GRBs. The at least nine satellites are considered to be placed on orbits with altitude of $\sim 500 - 600\,\mathrm{km}$ with inclination of $53°$ or at Sun-synchronous orbits of inclination $97.6°$.[2] One of the options for the *CAMELOT* satellite platform is the one being developed by C3S LLC in Budapest, therefore we apply its mass model in our Geant4 simulations.

The constellation of at least nine 3U CubeSats is proposed to be equipped with large and thin CsI(Tl) scintillators, of size $75 \times 150 \times 5$ mm^3 each, read out by Hamamatsu Multi-Pixel Photon Counters (MPPC). There would most likely be four scintillators on each satellite with two scintillators placed on two neighbouring sides of the satellite. The scintillators will be wrapped in the enhanced specular reflector (ESR) foil and enclosed in a support structure made either from aluminium or carbon fiber-reinforced plastic (CFRP). For details about the detector system see Ref. 187. The effective area of four detectors on board one *CAMELOT* satellite as a function of energy and for different directions, obtained from Geant4 simulations, is shown in Figure 18.

In order to understand and characterize the behaviour of the large-area CsI(Tl) scintillator detector and the MPPC readout, an experimental setup was built in Hiroshima, Japan. The experimental setup provided vital information for the simulation, mostly for the position dependence of the scintillator effective light yield. Different γ sources were used in the tests, mostly an ^{241}Am source.[188]

5 Validation of Geant4 Simulation and Calibration of Detector's Optical Parameters

A dedicated set of measurements were carried out with ^{241}Am γ source with an activity of 471 kBq which was collimated to irradiate different positions on the scintillator. The experiments were carried out with a single MPPC very similarly to the measurements presented in Ref. 188. The collimation was achieved with two lead sheets each containing holes in nine positions. In order to obtain the optical parameters of the scintillators as precisely as possible, the effect of reflectivity and absorption length on photon light yield was maximized by utilizing one MPPC in the middle of the shorter side of the scintillator. Spectra were recorded in nine cases by moving the ^{241}Am source
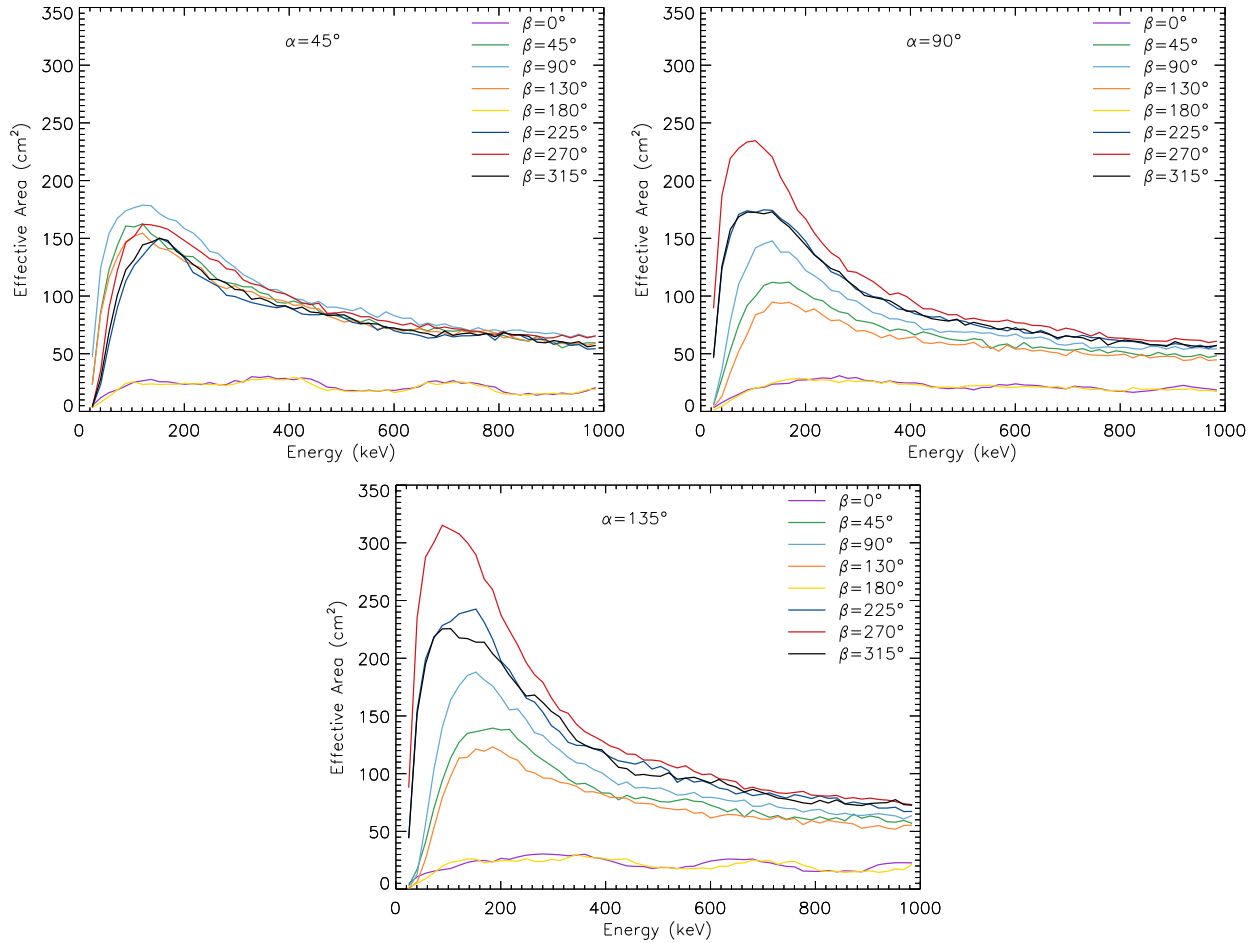
Fig 18 The effective area of four detectors on board one *CAMELOT* satellite as a function of energy and for different angles α and β defining the source direction in respect to the satellite. For the exact definition of these angles see Fig. 21.

in the nine positions where holes were present. Figure 19 shows the simulation of the experimental set-up.

The measured and simulated spectra for the irradiation point closest to the MPPC and in the farthest corner are compared in Figure 20. The same number of X-rays were simulated, which were emitted in 2 minutes of data acquisition for each spectrum. The difference between these spectra is the largest of all. The main reason for this is the difference in the mean path of optical photons, which is the shortest when the source is in front of the MPPC and the largest when the source is placed in the corner.
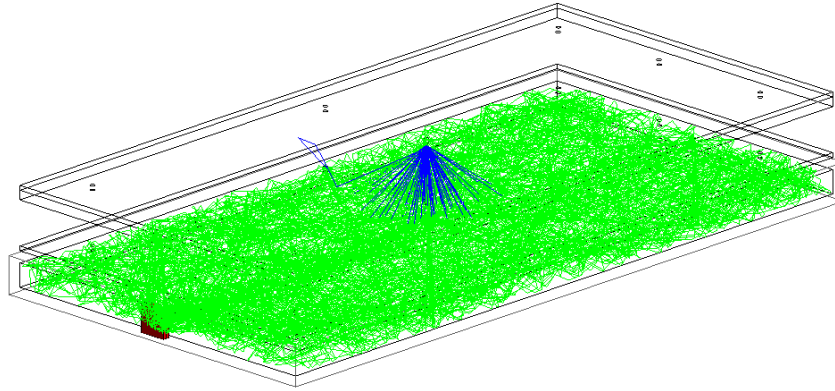
33

Fig 19 Simulation of 50 X-rays originating from a collimated X-ray source placed above the middle of the scintillator. Blue tracks are X-rays, green tracks are optical photons and the red square marks the MPPC. Only optical photons which are detected were drawn.

Two distinct peaks are visible in the measured and simulated spectra (Figure 20). The peak with the higher energy corresponds to the ^{241}Am γ peak at 59.5 keV. The lower-energy one is the K$_\alpha$ X-ray fluoresence peak of the Cesium in the scintillator.[188] The results of the Geant4 simulation were smeared by a Gaussian function with a standard deviation σ of 5 channels for the closest point of irradiation and 15 channels for the farthest to match them with the measured ones. The histogram of the number of photons detected in the simulation were scaled up by 1.35 and 1.39 respectively to match them with the measurements. This way assuming a linear detector response, all amplification factors were treated together. The fact that the scaling factor is almost the same for all parts of the scintillator translates to a good light collection efficiency. The main aim of the measurements was to determine the number of detected optical photons for an energy deposition of 1 keV in the scintillator (on average). For the measurements taken at the farthest position from the MPPC the 59.5 keV ^{241}Am peak was at ADC channel 180. The number of detected photons in the simulations had to be scaled up by roughly 1.37 to match the measurements. For the measurements taken at the closest point to the MPPC the same scaling parameter was used. For the farthest

position from the MPPC this implicates that an energy deposition of $1\,\text{keV}$ yields 4.11 detected optical photons on average.
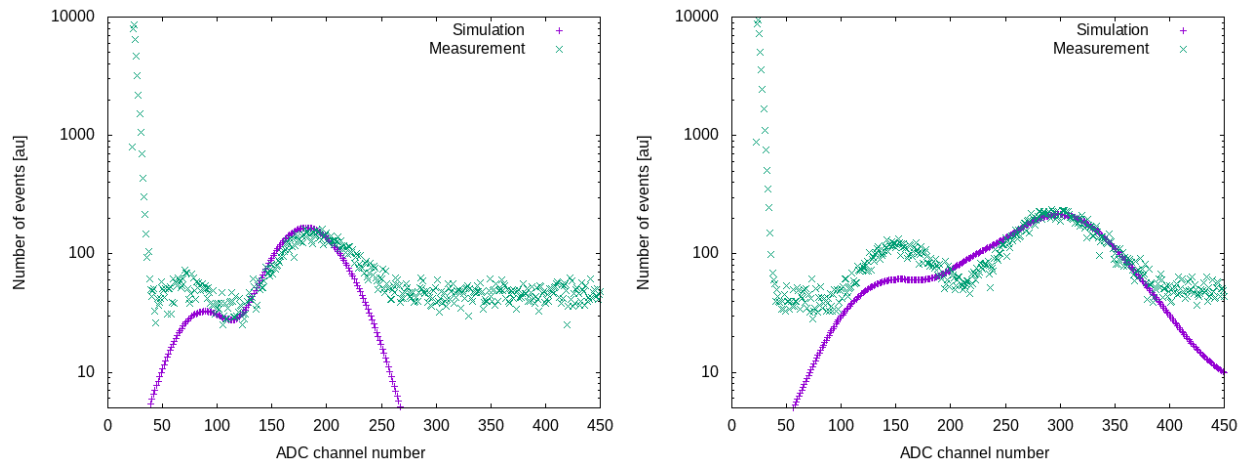

Fig 20 Simulated spectra of number of scintillation photons detected compared to the measurements. At the closest position to the MPPC (right) and at one of the farthest corners (left). The simulated spectra were smeard by 5 and 15 channels respectively.

The light yield in the simulation for the scintillator was fixed at 54 photons/keV, which is the yield for CsI(Tl) scintillators produced by Saint-Gobain[8] which is similar to our scintillator produced by AMCRYS[9]. The absorption length and the reflectivity of the surface of the scintillator was varied until the simulation agreed with the measurements for the two extreme spectra, the one in front of the MPPC and the one in the farthest corner. The best fitting reflectivity was $99.99\,\%$ and the absorption length determined from the fit was $60\,\text{cm}$. These values were used in the later simulations.

In this way of calibration the energy resolution and noise of the electronics are taken into account in the simulations. Although pileup is not included but during operation we do not expect such high count rates from regular sources where it could be relevant.

---

[8]https://www.crystals.saint-gobain.com/products/crystal-scintillation
[9]http://www.amcrys.com

6 Description of Geant4 Simulations

A Geant4 MC based simulation was developed in order to understand how the *CAMELOT* Cube-Sat constellation would detect γ-rays originating from short GRBs, long GRBs and TGFs. This required dedicated simulations of each background component as well as response to the γ-ray sources and calculation of the signal-to-noise ratio. The repository containing the simulation source code and analysis code are shared on GitHub (with a GNU General Public License). [10,11].

As the first step, the experimental setup that was used to calibrate the optical parameters of the CsI(Tl) scintillator – the γ-ray detector of the satellite – that with its casing was implemented in Geant4. Details are in Sec. 5. Afterwards the complex CAD model (Sec. 6.2) of the satellite – consisting of 7 modules, each with a given average material composition – was imported to Geant4 with CADMESH.[189] Four scintillators, each read out by 8 MPPCs were placed on two sides of the satellite.

In order to keep computation time at a reasonable level, the simulation of each primary particle is stopped if the number of detected optical photons reaches 10 000. Heavy ions can create several hundred thousands of scintillation photons. This limitation made it possible to run the codes on personal computers with a few cores. The signal of the 8 MPPCs is planned to be grouped into two groups of 4 MPPCs. In the following simulations the signal of all 32 MPPCs belonging to the four scintillators is summed up. This way we give a conservative signal-to-noise ratio (SNR) estimation since a more sophisticated trigger algorithm will decrease the chance of the background to exceed the threshold in each channel. The energy deposition is calculated from the number of detected optical photons. As described in Sec. 5, 1 keV energy deposition corresponds to 4.11 optical

---

[10]https://github.com/ggalgoczi/szimulacio/tree/master/Bck_4.10.6
[11]https://github.com/ggalgoczi/szimulacio/tree/master/GRB

photons detected in the simulation. This corresponds to an overall photon detection efficiency of 7% which is expected given the large size of the scintillator, the small sensitive area of MPPCs and the quantum efficiency of the MPPCs which depends on the scintillation light wavelength.

6.1 Directional and Positional Distribution of Primary Particles

The simulations presented in this paper can be split into two main groups based on whether we are simulating the source of the background or an astrophysical source. The latter are the target objects: sGRBs, lGRBs and TGFs, which can be considered as point sources very far away, therefore photons coming from these sources are treated in the simulations as parallel.

The other main group is the background (eg. CXB, albedo particles, trapped electrons). The background particles and γ-rays mainly hit the satellite from large solid angles or isotropically. The pointing strategy of the *CAMELOT* satellites is not established yet and the detector has all-sky FOV. We are interested in the estimation of a long-term average background at the regions of low geomagnetic latitude and outside SAA as mentioned in Sec. 3. Therefore, as an approximation, we assume that all components of the background flux of particles and γ-rays irradiate the satellite isotropically.

In order to realize this in the simulations the background particles were placed randomly on a sphere with a radius R around the model of the satellite. To maintain isotropy their direction was also randomly chosen. To boost up the simulation a source biasing was used[190] to limit the number of primary particles simulated to the ones which would hit the satellite. Due to the biasing, the number of detections in the simulation had to be normalized to determine the detection rate we would actually have.

The expected detection rate $N_{\text{det.rate}}$ for *CAMELOT* in space can be calculated as follows:[190]

$$N_{\text{det.rate}} = 4 f_\Omega \pi^2 R^2 (\sin^2 \theta_{\text{max}} - \sin^2 \theta_{\text{min}}) \Phi N_{\text{det.sim}} / N_{\text{prim}}, \qquad (16)$$

where $f_\Omega = \Omega/4\pi$ is the factor which takes into account the solid angle Ω of the type of the background. For instance albedo particles originate only from the atmosphere beneath the satellite. This corresponds to $3.95\,\text{sr}$ for our orbit. R is the radius of the sphere upon which the primary particles are distributed. This radius needs to be much larger than the size of the target object to maintain isotropy. θ stands for the angle that is formed by the initial direction of the simulated primary particle and the vector pointing to the center of the satellite from the origin of the simulated primary particle. By limiting θ we are able to simulate only those particles which would hit the satellite. In our case $R = 50\,\text{m}$. θ_{min} and θ_{max} are the upper and lower bounds for the chosen interval of the emission angle in the simulation. In our case $\theta_{\text{min}} = 0$ and $\theta_{\text{max}} = 0.5729°$. Φ is the flux in units of $\text{cm}^{-2}\text{s}^{-1}\text{sr}^{-1}$. $N_{\text{det.sim}}$ is the number of detections in the given simulation. N_{prim} is the number of primary particles shot in the simulation. The factor $\pi^2 R^2 (\sin^2 \theta_{\text{max}} - \sin^2 \theta_{\text{min}}) = 24668\,\text{cm}^2$. Table 2 summarizes the values of Ω and the normalization factor $f_{\text{norm}} = 4\Omega\pi^2 R^2 (\sin^2 \theta_{\text{max}} - \sin^2 \theta_{\text{min}})$ for the background models described in Sec. 3.

Table 2 Summary of solid angles Ω of background flux and normalization factor f_{norm}.

	CXB and primary CR	Galactic γ	Trapped and charged secondary particles	Albedo γ and n^0
Ω (sr)	8.64	0.542	4π	3.93
f_{norm} (cm^{2}sr)	8.525×10^5	5.348×10^4	1.240×10^6	3.878×10^5

In order to include all parts of the satellite including even the smallest volumes, the detailed CAD model of the satellite was read into Geant4 directly with CADMESH[189] that utilizes TETGEN[191] and ASSIMP[12] software libraries to directly read in STL files into Geant4. The satellite consists of seven modules including the structure of the satellite, the communications module, the payload etc. The only volume that was not included were the antennas. The material of each of the volumes was averaged (as described in Table 7. and Table 8.). The complete list of alloys used in each volume are listed in Sec. 10 together with their composition. Figure 21 shows the mass model of the *CAMELOT* satellite. Figure 30 in the Appendix presents the individual volumes of the satellite.

7 Results of Geant4 Simulations

7.1 Response to Each External Background Components

In this section the simulation results of the satellite response to each of 14 external background components is presented. The results are for one *CAMELOT* satellite. The count rate is summed for all detectors. By far the most relevant background is CXB. Therefore we chose to simulate two different CXB models introduced by Gruber et al. (1999)[105] and Ajello et al. (2008)[84] described in Sec. 3.1. The input energy spectra of each background component used for the simulations are described in the corresponding subsection of section 3. The model of the satellite was irradiated isotropically as shown in Figure 22.

Four possible aluminium detector support structure (shortly detector casing or just casing) thicknesses were investigated. The same material and thickness is on all sides of the detector housing, including the back side. In order to give an idea of the contribution of each component a
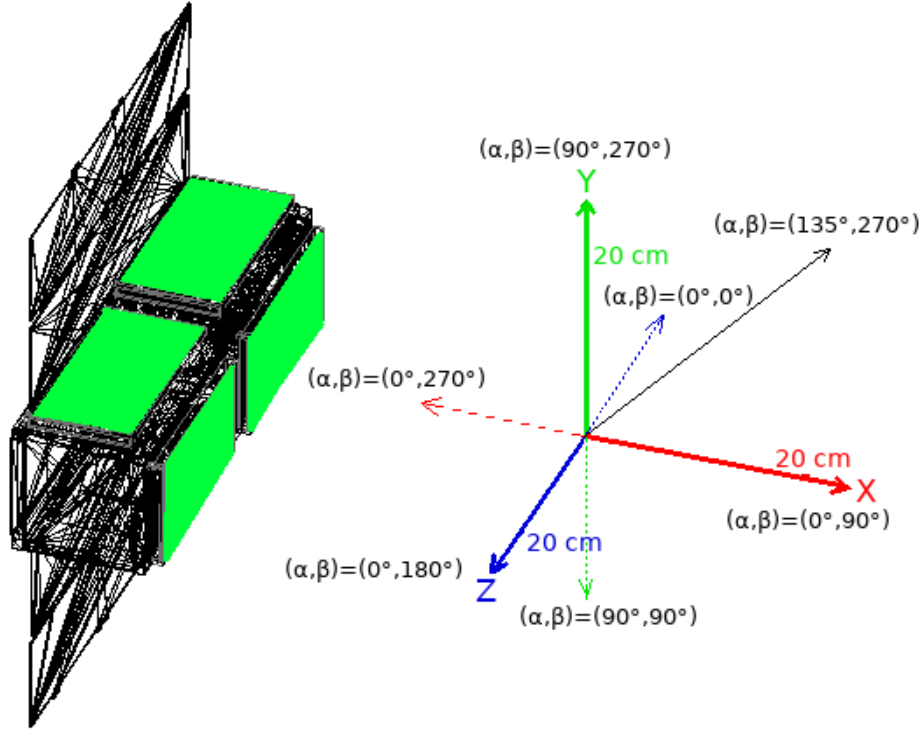
---

[12]http://www.assimp.org

Fig 21 The mass model used for the Geant4 simulations. The CAD model of the satellite was read into Geant4 and 4 scintillators (green rectangles) with their respective read out were placed on two sides of the satellite. The angles α and β refer to the angles shown in the figure of the detector's effective area. β is rotation around the Y axis, counted from the -Z axis and it increases towards +X axis. α is rotation around the Z axis, counted from the +X axis and increasing towards -Y axis. The highest effective area is for a source at direction $(\alpha, \beta) = (135°, 270°)$.

realistic 20 keV low-energy threshold was chosen. The five components which contribute the most to the background for the casing thickness of 0.5 mm thick Al with this low-energy threshold are: CXB ($\sim 1000-1100$ counts per second (cps)), albedo γ (~ 200 cps), primary CR protons (27 cps), albedo protons (45 cps) and albedo positrons (28 cps). Tables 3 and 4 summarize the background detection rate predicted by the simulation.

By summing up the contribution of each background component we derived a total background rate of 1550 cps for 0.5 mm, 1400 cps for 1 mm, 1270 cps for 1.5 mm and 1100 cps for 2 mm of the casing thickness assuming a low-energy threshold of 20 keV. From the two CXB models simulated, the Ajello et al. (2008) model was chosen since it gives a more conservative estimate. The Ajello et al. (2008) and Gruber et al. (1999) models have integral fluxes of 33.7 ph cm^{-2}s^{-1} and
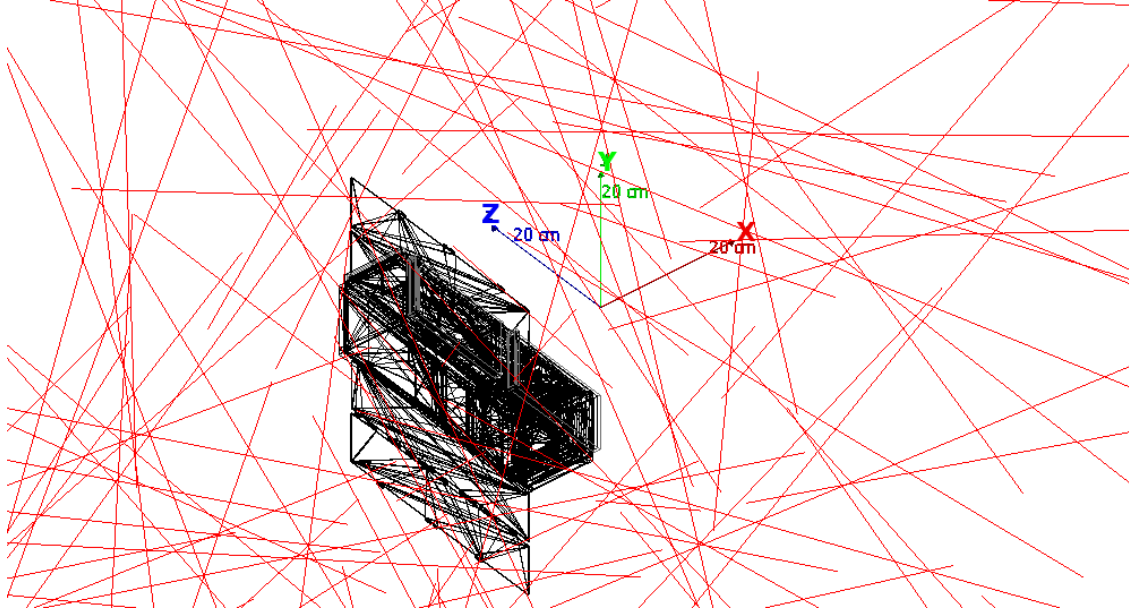
40

Fig 22 The mass model of the satellite is isotropically irradiated with X-rays (blue tracks). All four scintillators onboard appear green as they are filled with the tracks of optical photons which have green colour. The effect of the directional biasing (described in Sec. 6.1) can be seen.

Table 3 Simulated detection rate induced by cosmic and trapped particle background components.

Thickness (mm)	CXB A08	CXB G99	CR α	CR p^+	Galactic γ	Trapped p^+	CR e^-	CR e^+	Trapped e^-
0.5	1150	996	51	28	5.12	1.15	0.74	0.057	0.17
1.0	1020	893	49	29	3.98	0.947	0.76	0.057	0.073
1.5	890	770	51	29	4.04	0.820	0.76	0.060	0.072
2.0	858	707	51	29	3.50	0.827	0.75	0.059	0.066

The background detection rate is in counts per second, assumes a low-energy threshold of 20 keV, and is simulated for different thicknesses of the aluminium support structure of the detector. Two spectral models described by Gruber et al. (1999)[105] and by Ajello et al. (2008)[84] (denoted as G99 and A08) were simulated for the CXB. For the primary CR p^+ and α particles we used the ISO-15390 model with stormy magnetosphere and inclination of $i = 20°$. For primary CR e^- and e^+ we used the model described by Mizuno et al. (2004)[63] for solar minimum, $\theta_M = 29.6°$. For trapped e^- and p^+ we used the AE9 and AP9 models, respectively, for inclination of $i = 20°$, MC mode and derived from the 50 % CL of the fluxes. Altitude of 500 km was chosen.

30.3 ph cm^{-2}s^{-1} for $E > 10$ keV and give background rates of 1020 cps and 893 cps for 1 mm

thick Al detector casing, respectively.

The low-energy threshold onboard the *CAMELOT* satellites is planned to be a tunable pa-

rameter and changeable upon a ground command. Laboratory experiments show that low-energy

41

Table 4 Simulated detection rate induced by background components originating in the atmosphere.

Thickness (mm)	Albedo γ	Secondary e^+	Secondary e^-	Secondary p^+	Albedo n^0
0.5	208	28.2	6.32	45.5	23.8
1.0	205	27.1	8.00	43.7	22.3
1.5	192	27.4	7.95	42.5	22.3
2.0	191	28.2	7.86	43.4	21.4

The detection rate is in counts per second, assumes a low-energy threshold of 20 keV and is simulated for different thicknesses of the aluminium support structure of the detector. For secondary neutrons the spectrum for the solar minimum and for the cutoff rigidity $R_{\mathrm{cut}} = 5\,\mathrm{GV}$ was used.

threshold for our detectors is around $15 - 20\,\mathrm{keV}$. In Figure 23 the detection rate is shown for different casing thicknesses and low energy thresholds. The low energy part of the background spectrum is dominated by CXB X-rays which are stopped by thicker detector casing. The higher energy part is dominated mostly by hadrons and albedo gamma rays (hard spectrum) which can easily cross aluminium and deposit high energies in the scintillator.
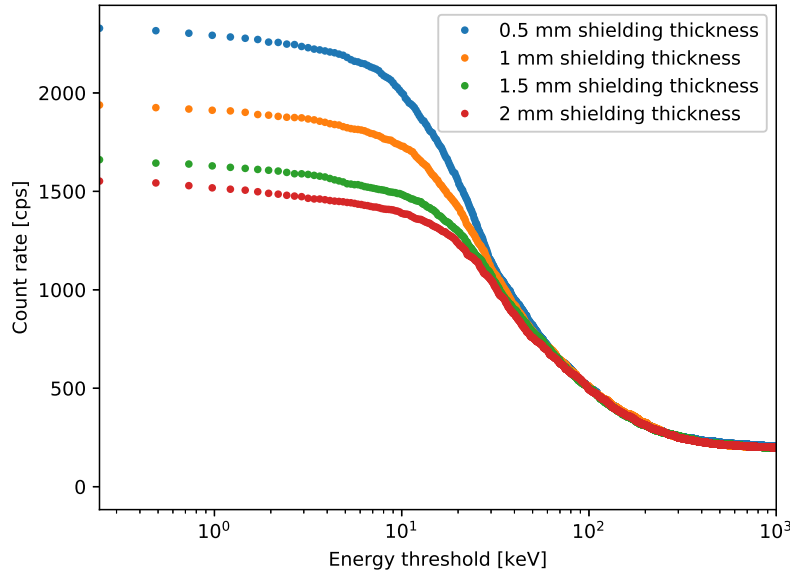

Fig 23 Background count rate for three aluminium detector support structure thicknesses versus low-energy thresholds. Above a threshold of $\sim$50 keV the thickness of the support structure does not change the background rate.

7.2 Simulation of a Typical Short GRB from Different Directions

In order to quantify if *CAMELOT* is capable of detecting X-ray sources we need to investigate the X-ray absorption by the satellite structures themselves. The four scintillators are placed on two sides of the satellite. Therefore the X-rays from half of the objects need to cross a certain part of the satellite before arriving to the detectors.
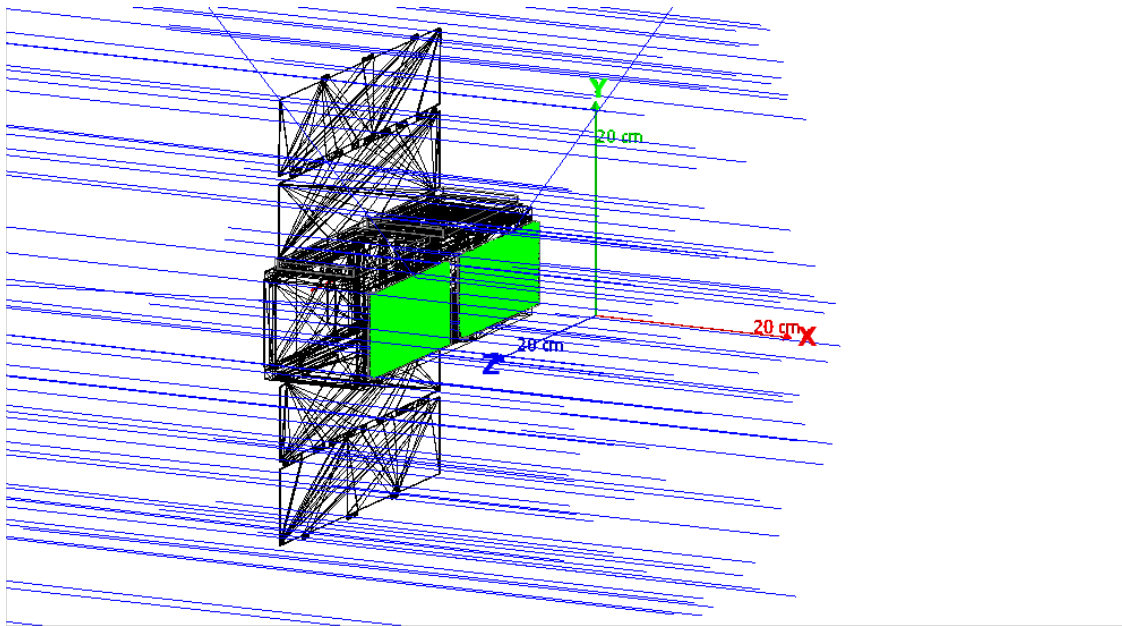

Fig 24 The satellite hit by parallel X-rays, such as the ones originating in short GRBs. Only one of the four scintillators were triggered in this case. Blue tracks are X-rays, green tracks are optical photons which were detected by the MPPCs.

To quantify the X-ray absorption of the satellite and to determine the count rate expected from sGRBs, different source directions were simulated. First, the satellite was rotated around its major axis by 10° 35 times to cover all directions around this axis. Afterwards the same was repeated for the minor axis of the satellite. A 1024 ms peak spectrum of a typical sGRB was used in the simulation. Details of typical sGRB spectra are described in subsection 2.1.

7.2.1 Rotating Around Major Axis for Short GRB

The satellite was rotated around its major axis (Z in Figure 24) by $10°$ between each simulation.

The simulated primary X-rays originated from the direction of the X axis. $0°$ case corresponds to

the scenario when X-rays arrive perpendicular to the surface of two of the scintillators. The count

rate is the highest for $45°$ when the angle between the direction of the photons and the surface

normal of both detectors is $45°$. The combined projected area of the four scintillators is the largest

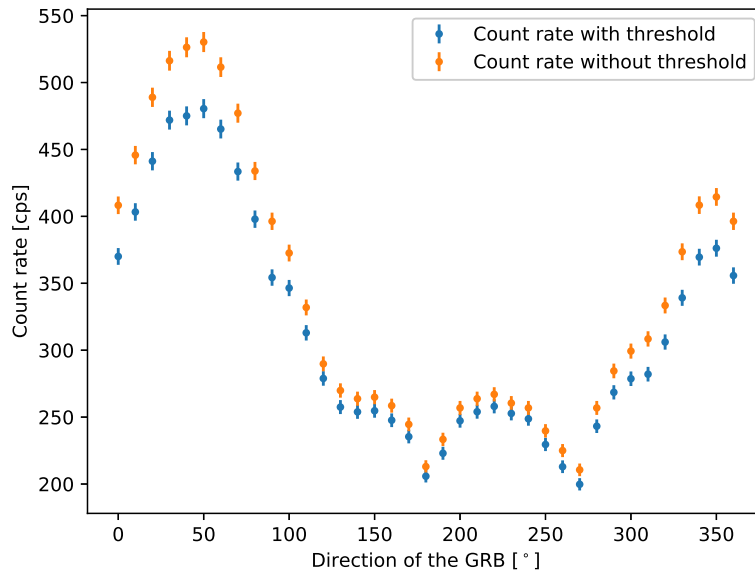in this scenario. The least favored direction is $270°$ (see Figure 25).

Fig 25 Count rate of a typical sGRB (for 1024 ms peak spectrum) for different source directions. The satellite was rotated around its major axis. An arbitrary but possible low-energy threshold of 20 keV was utilized. The detector support structure thickness of the scintillator was 2 mm.

In Figure 26 the spectra of two directions are shown. As expected for the least optimal direction

$(270°)$ the low energy part of the spectrum is suppressed. These are the X-ray photons which are

not able to cross the material of the satellite.

Different low-energy thresholds are possible to be set. Therefore, it is important to understand
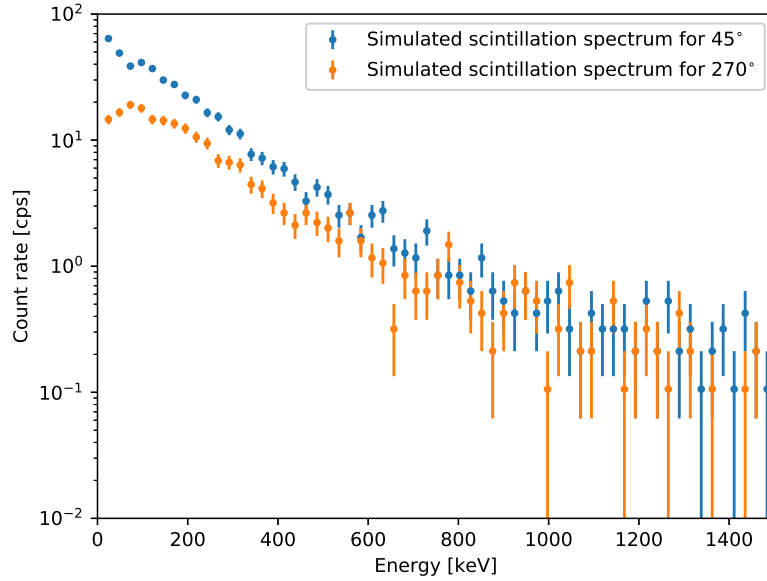
Fig 26 Typical short GRB spectra (for 1024 ms peak) for the most optimal direction and the least optimal direction among the investigated cases. The lower energy band is suppressed for 270°, since GRB X-rays need to cross the material of the satellite for this scenario to be detected. Thickness of the detector support structure was 2 mm in this case.

how the count rate of X-rays from sGRBs would change by varying the low-energy threshold. In Figure 27 the count rate for the most and least optimal direction is shown depending on the low-energy threshold. Up to about 100 keV the count rate does not decrease significantly. Also it is important to notice that the direction of the source is much more important than the thickness of the detector casing.

7.2.2 Rotating Around Minor Axis for Short GRBs

The same procedure as described in subsection 7.2.1 was followed for investigating sGRB (for 1024 ms peak spectrum) directions around the minor axis (X in Figure 24). X-ray were simulated as a parallel beam coming from the Z direction. In Figure 28 the count rate for each direction is shown. 0° is the least optimal. It corresponds to the case when all scintillators are seen from their edge. In this case the cross-section of the four scintillators combined is $7.5\,\mathrm{cm}^2$, which is about
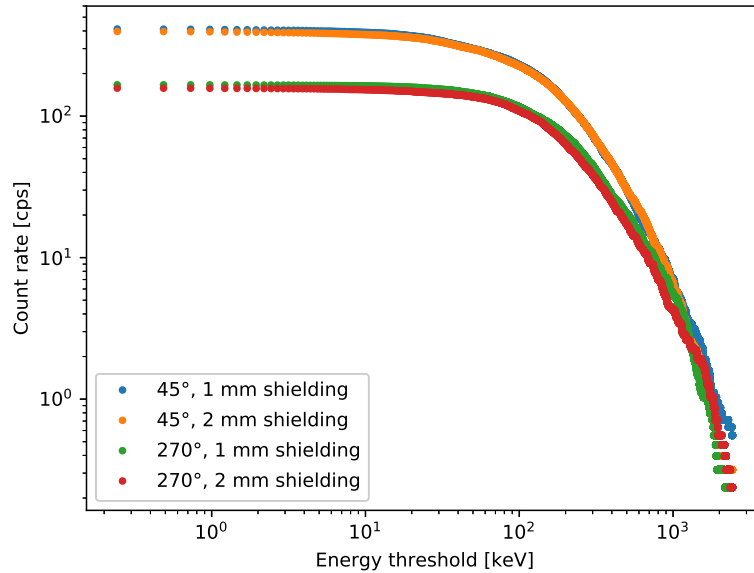
45

Fig 27 Count rate for a typical sGRB (for 1024 ms peak spectrum) versus detection low-energy threshold. Two source directions and thicknesses of the detector support structure are shown from the 70 investigated scenarios.

3 % of the area in the most optimal direction during rotation around the minor axis.

Since the background for the casing thickness of 2 mm is 1100 cps, a count rate of 165 cps is required from a sGRB to be observed with a significance of $5\,\sigma$. Therefore from the directions investigated with the rotation of the minor axis the interval between $50°$ and $150°$ is suitable for the detection of sGRBs.

7.3 Signal-to-Noise Ratio of X-ray/γ-ray Transients

For the detection of astrophysical objects, the final figure of merit is the SNR. It is important to mention that for the localization accuracy not only the SNR but also the number of detected photons is important for the cross-correlation of light curves. Electronic noise was neglected in the following calculations as the planned low-energy threshold set for detection is higher than the amplitude of the electronic noise.
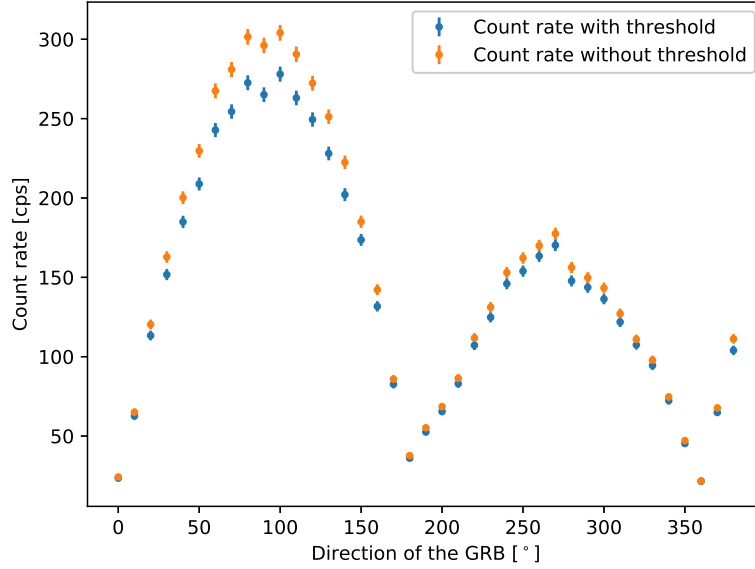
Fig 28 Count rate of a typical sGRB (for 1024 ms peak spectrum) for different source directions. The satellite was rotated around its minor axis. An arbitrary but possible low-energy threshold of 20 keV was utilized. The aluminium detector support structure was 2 mm thick in this case.

Detection low-energy threshold can be set onboard the satellite. Therefore SNR was quantified for each astrophysical object in the function of low-energy threshold. The following equation was used to determine SNR:

$$SNR = \frac{\Delta t \sum\limits_{E_1}^{E_2} f(E)}{\sqrt{\Delta t \sum\limits_{E_1}^{E_2} g(E)}},$$ (17)

where $f(E)$ is the detected count rate spectrum of the signal, $g(E)$ stands for the detected count rate background spectrum, E_1 is the low-energy threshold, E_2 is the high-energy threshold and Δt is the exposure time. In our simulations we did not put boundary on the high-energy threshold, but the triggering algorithm onboard *CAMELOT* satellites will have capability to set both the low- and the high-energy thresholds.

The main aim of the *CAMELOT* mission is the detection and localization of sGRBs. Therefore it is important to understand with what significance could *CAMELOT* satellites detect these objects. Among the direction, when the satellite was rotated around its major axis SNR is the highest when the angle between X-rays from a GRB and the surface normal of both detectors is $45°$. We have the lowest SNR for the angle of $270°$ (see Figure 25).
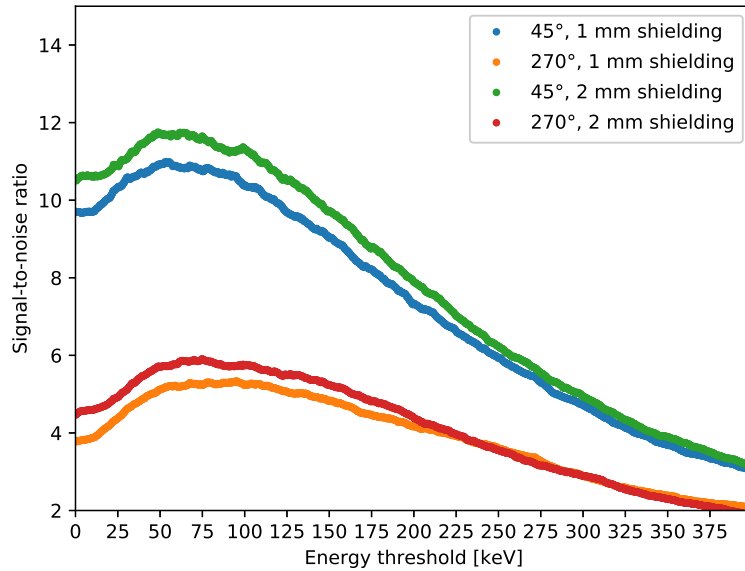
Fig 29 Signal-to-noise ratio of short GRBs versus low-energy detection threshold. Two detector support structure thicknesses and two GRB directions (rotating around Z axis) are shown among the directions investigated in Sec. 7.2.1. Among these investigated directions, highest signal is achieved when the direction of the GRB is $45°$. For $270°$ the signal from a typical sGRB is the smallest (see Figure 25).

When the simulated typical sGRB (for $1024\,\mathrm{ms}$ peak spectrum) is in the most optimal direction an SNR of > 11 can be achieved. SNR stays above 10 within the low-energy detection threshold range from up to $100\,\mathrm{keV}$. The thickness of the aluminium detector casing affects SNR mostly for low values of the low-energy detection thresholds, since the main background component, CXB has a rather soft spectrum. For the least optimal direction among the directions investigated an SNR of 6 can be achieved. This characteristic is shown in Figure 29. The other directions, when

48

the satellite was rotated around its minor axis (Figure. 28), are less favored. In these cases the cross section of the detectors are significantly lower.

Tables 5 and 6 summarize the simulated detection count rate induced by the X-ray/γ-ray transient sources and the expected SNR. For GRBs four different exposure times Δt were used: 64, 256 and 1024 ms for sGRBs and 4096 ms for lGRBs. It should be noted that long triggering timescales of the order of several seconds or tens of seconds are readily affected by the time variation of background due to geomagnetic latitude (cutoff rigidity) change during the orbit and the activation background varying with time since SAA passages. The SNR calculated for such long integration time is effected by the background systematics. Varying background can cause false triggers and detectors with larger effective area are more vulnerable unless a sophisticated background modeling is part of the trigger algorithm.

Different missions has employed different triggering timescales. *BeppoSAX*/GRBM used adjustable timescale in the range from 7.8125 ms to 4 s in 10 steps.[192] *CGRO*/BATSE used time windows of 64 ms, 256 ms and 1024 ms.[193] *Suzaku*/WAM used triggering timescales of 1/4 s and 1 s.[21] *HETE-2*/WXM and FREGATE used timescales from 80 ms up to 10.5 s or longer, but they modeled background to remove trends which can cause false triggers.[194] *Swift*/BAT uses two types of rate triggers: i) "short" rate triggers with timescales 4, 8, 16, 32 and 64 ms which are traditional triggers employing single background period of fixed duration; ii) "long" rate triggers with timescales from 64 ms to 64 s which fit multiple background intervals to remove trends as pioneered by *HETE-II*.[195] *Fermi*/GBM uses triggering timescales of 16, 32, 64, 128, 256, 512, 1024, 2048, 4096 and 8192 ms.[26] In case of *AGILE*/MCAL, transients are searched using time windows of duration of sub-millisecond, 1, 16, 64 , 256, 1024 and 8192 ms.[196,197]

From Table 6 it is also seen that in contrary to one's expectation, TGF SNR increases with

thicker detector casing. The reason for this is the hardness of TGF spectrum. The median energy of X-ray photons originating in TGFs is 2 MeV. These have a few per cent chance to interact with the scintillator material. The thicker detector casing provides more material in which these energetic photons can interact and produce secondary particles. Therefore thicker casing yields in higher SNR. This study is important in order to understand sensitivity of different trigger time window durations necessary for designing efficient GRB trigger algorithm.

Table 5 Simulated detection rate induced by X-ray/γ-ray transient sources.

Al	sGRB peak spectrum			lGRB peak spectrum			lGRB fln. sp.	TGF	SGR
(mm)	64 ms	256 ms	1024 ms	64 ms	256 ms	1024 ms			
0.5	1440	910	385	1190	924	758	326	34600	16200
1.0	1390	911	367	1139	908	715	309	38900	14000
1.5	1300	890	367	1110	840	674	292	37600	11900
2.0	1320	839	355	1058	815	662	277	38600	10500

The detection rate is in counts per second, assumes a low-energy threshold of 20 keV and is simulated for different thicknesses of the aluminium support structure of the detector. For short and long GRBs the 64 ms, 256 ms and 1024 ms peak spectra were used. For long GRB also the fluence spectrum (fln. sp.) was used.

Table 6 Simulated detection signal-to-noise ratio for X-ray/γ-ray transient sources.

Al	sGRB peak spectrum			lGRB peak spectrum			lGRB fln. sp.	TGF	SGR
(mm)	64 ms	256 ms	1024 ms	64 ms	256 ms	1024 ms	4096 ms	0.1 ms	0.2 s
0.5	9.27	11.7	9.91	7.66	11.9	19.5	16.8	8.79	185
1.0	9.35	12.3	9.87	7.66	12.2	19.2	16.7	10.3	167
1.5	9.23	12.6	10.4	7.89	11.9	19.2	16.6	10.6	149
2.0	10.1	12.8	10.8	8.08	12.5	20.2	16.0	11.6	142

The detection SNR has been calculated for different thicknesses of the aluminium support structure of the detector. The assumed background count rate is the sum of all components as described in Ref. 7.1. For the GRB peak spectra were used the exposure time $\Delta t = 64$ ms, 256 ms and 1024 ms. For the fluence spectrum (fln. sp.) of long GRB we used $\Delta t = 4096$ ms. For TGF we assume exposure time $\Delta t = 0.1$ ms and for SGR $\Delta t = 0.2$ s. For this TGF spectrum the SNR is only a theoretical value following from the formula. For example, for 1 mm thicknesses of the Al detector casing the expected detected number of counts within 0.1 ms from is 3.9 cnt, whereas the expected number of background counts is below 1 cnt (only 0.14 cnt).

8 Discussion

The background count rates obtained in our MC simulations were derived from models of fluxes of gamma-rays and particles averaged over various latitudes, depending on the particular flux component, below $50°$ and outside SAA. The reason is that we aim to obtain an expected "mean" background rate in parts of orbit which are suitable for gamma-ray transient scientific data collection. However, in reality, the background rate will have time variation due to geomagnetic latitude (cutoff rigidity) change within the orbit and due to the activation background varying with time since SAA passages.

The foreseen orbital inclination of the *CAMELOT* satellites is above $\sim 50°$ and option of polar orbits is also likely. Therefore significant background variation is expected as well. We investigated background count rates measured by *Fermi*/GBM, *RHESSI*[198] and *Lomonosov*/BDRG[131] gamma-ray instruments throughout their orbits to learn what background variations are expected. In case of *Fermi*/GBM (altitude $560\,\mathrm{km}$ and inclination $26°$) the background rate outside SAA for one NaI detector module in $8 - 1000\,\mathrm{keV}$ range varied throughout the orbit between $\sim 1000\,\mathrm{cps}$ and $\sim 1500 - 2000\,\mathrm{cps}$, i.e. $\sim 1.5 - 2\times$ change (about two months after the launch), see also Ref. 199. In case of the *RHESSI* spectrometer (altitude $500\,\mathrm{km}$ and inclination $38°$) the background rate outside SAA for one rear detector segment in $25 - 20\,000\,\mathrm{keV}$ range varied throughout the orbit between $\sim 250\,\mathrm{cps}$ and $\sim 650\,\mathrm{cps}$, .i.e. $\sim 2.5\times$ change (about three years after the launch) [13]. For a detector on a polar orbit the background rate can increase dramatically more when passing the polar regions of trapped particles in the van Allen radiation belt. The *Lomonosov*/BDRG (altitude $550\,\mathrm{km}$ and inclination $98°$) measurements show that the rate outside SAA, in $20 - 450\,\mathrm{keV}$ range increases $\sim 50\times$ inside the polar regions compared to the rates near equator (about 5 months

---

[13]http://sprg.ssl.berkeley.edu/~tohban/browser/

after the launch), see also Ref. [131]. Therefore outside SAA and polar trapped particle regions the background count rate variation of at least $\sim 2\times$ the value near the equator for detectors on board the *CAMELOT* satellites are also foreseen. Inside the polar regions the rate increase can be much higher.

Since CubeSats which are not on equatorial orbit (currently most of them) are subject to high proton flux upon SAA passages, these protons have enough energy to activate the material of the satellite.[69] Short term activation is important as decaying isotopes can cause a strongly time-variable background for a few minutes after the end of SAA passes. Long term activation can increase the background significantly in a matter of months.[200] To quantify the effects of proton induced activation, we plan to conduct simulations in the near future. Emission lines of radioactive isotopes could also be used for energy calibration. As an example for our scintillators ^{123}I will be created which emit γ-rays with an energy of 159 keV.[201]

In order to discuss how our estimated background rates of *CAMELOT* detectors scale to the observations of *Fermi*/GBM, *AGILE*/MCAL and *Suzaku*/WAM we consider the surface area of the scintillators of these instruments and assume that these surface areas can be used as rough scaling factors. For CAMELOT (CsI): $15\,\text{cm} \times 7.5\,\text{cm} \times 4$ scintillators giving the area of $\sim 450\,\text{cm}^2$. For *Fermi*/GBM (NaI): $3.14 \times (12.7/2\,\text{cm})^2$ giving the area of $\sim 127\,\text{cm}^2$ for one detector module (the effective area around 0.4 MeV is $\sim 30\,\text{cm}^2$).[202] For *AGILE*/MCAL (CsI): $1.5\,\text{cm} \times 37.5\,\text{cm} \times 30$ detectors giving the area of $\sim 1700\,\text{cm}^2$ (the effective area at $0.4 - 1\,\text{MeV}$ is $\sim 200 - 300\,\text{cm}^2$).[54] For *Suzaku*/WAM (BGO) the area is $\sim 800\,\text{cm}^2$.[21]

The estimated background rates of *CAMELOT* detectors for 0.5 mm Al support structure are ~ 2.3, ~ 0.75 and ~ 0.3 kHz respectively for $E > 10\,\text{keV}$, $E > 50\,\text{keV}$ and $E > 400\,\text{keV}$ (see Fig. [23]). The observed background rates of one detector module of *Fermi*/GBM (~ 2 months

after the launch, altitude $h = 560\,\text{km}$ and inclination $i = 26°$) are $\sim 1\,\text{kHz}$ and $\sim 0.13\,\text{kHz}$ for $E > 10\,\text{keV}$ and $E > 400\,\text{keV}$, respectively. For *AGILE*/MCAL ($h = 550\,\text{km}$ and $i = 2.5°$) the rate is $\sim 1.3\,\text{kHz}$ for $E > 400\,\text{keV}$. In case of *Suzaku*/WAM ($h = 570\,\text{km}$ and $i = 31°$) the rate is $4 - 6\,\text{kHz}$ for $E > 50\,\text{keV}$.

If we use the surface area of scintillators as a scaling factor than the background rate scaling between *Fermi*/GBM and *Suzaku*/WAM or *Fermi*/GBM and *AGILE*/MCAL is in a good approximation. The current simulated *CAMELOT* background is smaller than that of *Fermi*/GBM and *Suzaku*/WAM observations. For example, if we scale the *CAMELOT* background to the *Fermi*/GBM, it would be $\sim 0.65\,\text{kHz}$, which is lower than the observed value of $\sim 1\,\text{kHz}$ for $E > 10\,\text{keV}$. This is of course due to the activation background component, which is not included in the *CAMELOT* simulated background and the scaling would be reasonable if we consider the activation background component for *CAMELOT* around $1 - 2\,\text{kHz}$. The same applies when we scale *CAMELOT* background to *Suzaku*/WAM observations. Scaling *CAMELOT* background to *AGILE*/MCAL is in a good agreement even without accounting for the activation component for *CAMELOT*. The *AGILE*/MCAL satellite is in an equatorial orbit with an inclination of only $2.5°$ with low particle background which causes material activation.

Having the simulation results of the detection background count rate and GRB count rate we can discuss an approximate number of expected short and long GRB detections per year by a single *CAMELOT* satellite. For 1 mm Al casing and the best gamma-ray incident angle ($45°$ to the surface normals of perpendicular detectors) the simulation detection count rate is $911\,\text{cps}$ and $715\,\text{cps}$ for sGRB $256\,\text{ms}$ and lGRB $1024\,\text{ms}$ median peak spectrum, respectively. GRBs will not always be seen under this most preferred direction therefore we scale this rate by a factor of $1/\sqrt{2}$ which corresponds to the rate expected from GRBs seen perpendicular to the largest

scintillator side (644 cps for sGRB and and 506 cps for lGRB). There will be GRBs seen under more preferred direction as well as under less preferred direction therefore this is a compromise direction. Furthermore we can assume a detection SNR threshold to be 5 and a mean background count rate to be 3 000 cps (1 500 cps from external background flux and 1 500 cps from material activation).

Therefore for the above-mentioned integration times we obtain detection count rate thresholds of 541 cps and 271 cps, respectively for sGRBs and lGRBs with median spectral shapes. By scaling the spectral normalizations A_{256} and A_{1024} of typical *Fermi*/GBM sGRB and lGRB from Table 1 by factors of $541/644$ for sGRB and by $271/506$ for lGRB and by integrating those amplitude-scaled typical spectra one obtains the threshold photon peak fluxes of 4.03 ph cm^{-2}s^{-1} for sGRB (or fluence of 3.92×10^{-7} erg cm^{-2} for 256 ms) and 2.22 ph cm^{-2}s^{-1} for lGRB (or fluence of 3.48×10^{-7} erg cm^{-2} for 1024 ms). These thresholds together with the expected duty cycle can be used to estimate an approximate number of GRB detections per year from the distribution of GRB photon peak fluxes from the FERMIGBRST catalog.

Fermi/GBM surveys the entire sky, that is not occulted by the Earth, with the observing duty cycle of $\sim 85\,\%$.[203] Following the trapped particle maps the duty cycle would be 76 % for orbital inclination of $89°$ (polar orbit is an option for *CAMELOT* CubeSats) and integral particle flux $\leq$ 10 particle cm^{-2}s^{-1} (see Sec. 3.3 and Ref. 150). However, we examined background data measured by a GRB instrument *Lomonosov*/BDRG at polar LEO and it suggests that due to high background variation the duty cycle can be expected to be lower, i.e. about $60\,\%$. Therefore we assume this more conservative value of $\sim 60\,\%$ as a duty cycle for a single *CAMELOT* CubeSat. From these calculations we obtain an approximate number of sGRBs detectable by a single *CAMELOT* CubeSat, i.e. with photon peak flux higher than the aforementioned thresholds, to be 18/year. In

case of lGRBs we obtained 115/year.

In the same way we proceeded with SGRs. By using the simulated detection count rate of a typical SGR for the aluminium detector casing thickness of 1 mm from Table 5 and the typical SGR spectral parameters calculated in Sec. 2.2 we obtained SGR detection threshold photon flux of $9.19 \, \mathrm{ph \, cm^{-2} s^{-1}}$ or threshold fluence of $8.47 \times 10^{-8} \, \mathrm{erg \, cm^{-2}}$ for $0.2 \, \mathrm{s}$ and energy range of $15 - 500 \, \mathrm{keV}$. This means that all bursts listed in the Konus catalog of SGRs between 1978 and 2000[44] would be detectable also by a *CAMELOT* CubeSat.

A difficulty is to estimate the SGR annual detection rate using this catalog because it was composed of measurements from several interplanetary spacecrafts and one LEO satellite which means it is difficult to know the exact duty cycle for the SGR measurements. Therefore we examined the five year *Fermi*/GBM SGR catalog[204] and calculated the detection thresholds also for the time scale of $0.1 \, \mathrm{ms}$ and energy range of $8 - 200 \, \mathrm{keV}$ which are the median SGR duration and energy range used in this catalog. For these conditions we obtained *CAMELOT* SGR photon flux detection threshold of $18.2 \, \mathrm{ph \, cm^{-2} s^{-1}}$ or fluence threshold of $5.82 \times 10^{-8} \, \mathrm{erg \, cm^{-2}}$. Using this fluence threshold, the SGR fluence distribution reported in the *Fermi*/GBM SGR catalog and the aforementioned assumed duty cycle of a single *CAMELOT* CubeSat we obtained a prediction of 46 SGRs detectable by one *CAMELOT* satellite annually. Note that the annual number of detected SGRs will be subject to large fluctuations since SGR bursts tend to occur in clusters when particular magnetars become active.

Concerning the used SNR calculation it should be noted that it is rather simplistic for TGF detection. The large number of $0.1 \, \mathrm{ms}$ intervals (large number of trials) during the mission examined by the trigger algorithm (note that the rate trigger algorithm for *CAMELOT* is yet under development) as well as the fact that a cosmic ray could easily cause a count in two detectors needs to be

taken into account. If other background sources by chance produce one or two additional counts in the same 0.1 ms interval, then a false trigger would be issued.

Specific conditions of the trigger algorithm to efficiently detect TGFs by *CAMELOT* CubeSats are yet to be determined. For example one option is to aim to detect brighter but less frequent TGFs. *AGILE*/MCAL observes 2780 TGFs within 3.5 years which is ~ 800 TGFs/year.[55] The fluence distribution follows a power low of -2.2.[57] This means that TGFs with 5 times greater fluence will be 3 % in number. The spectrum of a typical TGF used in our simulations is based on the TGF fluence at the threshold level of *AGILE*/MCAL. Therefore if a *CAMELOT* satellite had equtorial orbit as *AGILE* then this scaling would give 23 TGFs/year/CubeSat with 19.5 cnts/TGF.

However, *CAMELOT* satellites will likely have polar or other high-inclination orbits. From observations most, if not all, TGFs has been detected at latitude lower than $45°$ north and south by *CGRO*/BATSE, *RHESSI*, *AGILE*/MCAL, *Fermi*/GBM and ASIM instruments.[205,206] One of the good distribution maps[205] was obtained from the recent ASIM instrument.[207] As relatively young (operational for ~ 2 years yet), the TGF number is not high, but with $51.6°$ on *ISS*, it has a relatively uniform coverage of the TGF positional distribution. There are three major TGF sites: around Central America, around Central Africa and around South East Asia. A good comparison of the expected TGF detections by *CAMELOT* can be done with the *TARANIS*/XGRE instrument which was supposed to operate on Sun-synchronous orbit with 700 km altitude. According to Ref. 208 *TARANIS* (unfortunately lost due to the VEGA launch failure) was expected to detect ~ 200 TGFs/year. A *CAMELOT* satellite will have about 1/10 of the effective area, but if corrected for the 500 km vs. 700 km altitude difference, this would be converted into $\sim 1/5$. Then 200×3 % (for $5\times$ brighter TGFs) give ~ 6 TGFs/year for a single satellite. With 9 satellites in a constellation CAMELOT would provide ~ 50 TGFs/year.

As shown in Fig. 25, the *CAMELOT* detectors can observe gamma-ray sources also for directions when the photons need to pass through the body of the satellite (rear direction). This means that also gamma-ray photons scattered off the Earth's atmosphere and entering the detector from the side not facing the source can produce signal. In this sense the *CAMELOT* satellites will have omnidirectional FOV although the sensitivity for the rear direction is lower. Compton scatter of the burst flux off the Earth's atmosphere into the detector is known effect and observed already by the *CGRO*/BATSE instrument.[209] Correction for this effect has been included in the BATSE's response matrices[210] and in the trigger efficiency calculation.[211] See also Refs. 212, 213 with spectrum of GRB 021206 measured by the RHESSI satellite which shows significant Earth's atmospheric backscatter of photons below 300 keV. Moreover, a method which employs the atmospheric scattering of GRB flux for the polarisation measurements in the prompt gamma-ray emission has been published in Ref. 214 and Ref. 215. The atmospheric scattering might affect the *CAMELOT* measurements and it might be necessary to do careful modeling of this effect in the future in order to reduce the systematic uncertainties. A detailed simulation of this effect is beyond the scope of this paper, however such an analysis might be useful to improve the timing based localization in LEO.

9 Conclusions

A Geant4 based simulation was developed to understand the capabilities of the planned *CAMELOT* CubeSat constellation to detect short and long GRBs, TGFs. The CAD model of the satellite was imported directly to Geant4 with CADMesh. Since the scintillators onboard *CAMELOT* have a considerably large size, optical light propagation is important. To take this into account, scintillation light propagation was simulated in Geant4 by tracking each optical photon created by

scintillation.

The simulation was validated and its optical parameters were calibrated with an ^{241}Am X-ray source. The calibrated reflectivity of the surface of the scintillator turned out to be 99.99 % and absorption length 60 cm.

Thirteen background components were simulated to determine their contribution to the overall background spectrum. The five components which contribute the most to background are: CXB (1000 cps), albedo X-rays (200 cps), cosmic-ray α particles (49 cps), albedo protons (44 cps) and albedo positrons (27 cps). These count rates were calculated by assuming a 20 keV low-energy threshold and 1 mm of aluminium detector support structure thickness.

The total simulated background rate was 1545 cps for a detector casing thickness of 0.5 mm. By increasing the casing thickness to 1 mm the total background decreased to 1410 cps and by increasing it more to 1.5 mm it turned out to be 1270 cps. Finally for 2 mm it was 1100 cps. These rates were obtained from models of fluxes of gamma-rays and particles averaged over various latitudes, depending on the particular flux component, below $50°$ and outside SAA, because our goal was to obtain an expected "mean" background rate in parts of orbit which are suitable for gamma-ray transient scientific data collection.

Since the four scintillators of the *CAMELOT* CubeSat are placed on its two sides the direction of the source influences the signal-to-noise ratio. A typical short GRB was simulated in 70 directions. 35 directions were investigated by rotating the satellite around its major axis by $10°$ between simulations. The SNR of the detection of the typical short GRB (with integral fluxes between 8.15 ph cm^{-2}s^{-1} and 2.21 ph cm^{-2}s^{-1} for $E > 5$ keV and for 64 and 1024 ms integration window respectively) varied between 5 and ~ 10. Other 35 directions were simulated by rotating the satellite around its minor axis. This resulted in less favorable directions, since the cross section

with respect to the direction of X-rays from the sGRB is much smaller in this case. An SNR of at least 5 was determined for the range from 50° to 150°.

The simulations show that CubeSats equipped with large area scintillators are able to detect sGRBs, lGRBs, TGFs and SGRs. In our case for the *CAMELOT* CubeSats an average sGRB (256 ms peak spectrum) could be detected with an SNR of > 12 in the most favoured direction. lGRBs (with an integral flux of $2.54 \, \mathrm{ph \, cm^{-2} s^{-1}}$ for $E > 5 \, \mathrm{keV}$) yield an SNR of > 16 for 4096 ms exposure. TGFs despite their very short duration of 0.1 ms could also be detected because, for example, for 1 mm thicknesses of the Al detector casing the expected detected number of counts within 0.1 ms from a TGF (with fluence at the threshold level of *AGILE*/MCAL) is 3.9 cnt, whereas the expected number of background counts is only 0.14 cnt. SGRs due to their very large X-ray flux yield in an SNR of >100. The results of the simulation will aid the development of the trigger algorithm and also choosing the detector support structure.

to thank at last but not least the engineers at C3S LLC for the support they provided with the CAD

model of the satellite.

10 Appendix

Table 7 The mass ratio of materials that are used for the satellite (Courtesy of C3S LLC).

Name of module	mass [g]	Type of material	Mass ratio [%]
ADCS	710	Aluminum 6061-T6	50
		Copper Electric	25
		Glass Borosilicate	25
COM	90	Stainless Steel	2
		Brass Generic	25
		Aluminum 7075-T73	40
		FR4 Glass-Epoxy sheet	33
EPS	750	FR4 Glass-Epoxy sheet	25
		Aluminum 6061-T6	75
OBC	50	FR4 Glass-Epoxy sheet	100
STRU	980	Aluminum 6061-T6	100
SP	570	Solar Panel	100
Payload	100	Aluminum 7075-T73	100

Table 8 The chemical composition of materials in mass fraction that are used for the satellite (Courtesy of C3S LLC).

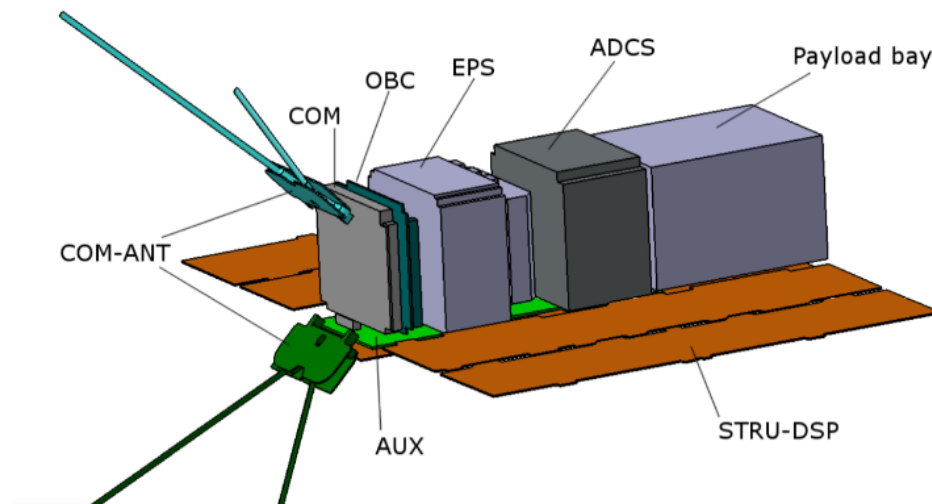| Material name												
Aluminum 6061-T6	Al	96.90	Mg	1.20	Si	0.80	Fe	0.70	Cu	0.40		
Aluminum 7075-T73	Al	88.60	Zn	6.10	Mg	2.90	Cu	2.00	Si	0.40		
Stainless Steel	Fe	66.50	Cr	20.00	Ni	10.50	Mn	2.00	Si	1.00		
Copper Electric	Cu	100.00										
Glass Borosilicate	Si	42.10	O	54.80	B	3.10						
FR4 Glass-Epoxy	Si	23.39	O	36.02	C	37.04	H	3.55				
Brass Generic	Cu	85.00	Zn	15.00								
Solar Panel	Ge	38.00	Si	24.00	O	20.00	C	13.00	H	4.00	B	1.00

Fig 30 The individual volumes of the simulated satellite. The CAD model of the satellite was read into Geant4 and 4 scintillators (not displayed on this figure) with their respective read out were placed on two sides of the satellite (Courtesy of C3S LLC).

References

1 J. Allison, K. Amako, *et al.*, "Recent developments in Geant4," *Nuclear Instruments and Methods in Physics Research Section A: Accelerators, Spectrometers, Detectors and Associated Equipment* **835**, 186–225 (2016).

2 N. Werner, J. Řípa, A. Pál, *et al.*, "CAMELOT: Cubesats Applied for MEasuring and LOcalising Transients mission overview," in *Proceedings of the SPIE*, *Society of Photo-Optical Instrumentation Engineers (SPIE) Conference Series* **10699**, 106992P (2018).

3 A. Pál, L. Mészáros, N. Tarcai, *et al.*, "CAMELOT - Concept study and early results for onboard data processing and GPS-based timestamping," *arXiv e-prints* , arXiv:1806.03685 (2018).

4 J. Řípa, N. Werner, M. Ohno, *et al.*, "Monitoring of gamma-ray bursts with a fleet of nanosatellites," in *69th International Astronautical Congress*, IAC–18,B4,2,8,x46335 (2018).

5 J. Smith, "BurstCube: Mission Concept, Performance, and Status," in *36th International Cosmic Ray Conference (ICRC2019)*, *International Cosmic Ray Conference* **36**, 604 (2019).

6 J. S. Perkins, J. Racusin, M. S. Briggs, *et al.*, "BurstCube: A CubeSat for Gravitational Wave Counterparts," in *35th International Cosmic Ray Conference (ICRC2017)*, *International Cosmic Ray Conference* **301**, 760 (2017).

7 T. Chattopadhyay, A. D. Falcon, D. N. Burrows, *et al.*, "BlackCAT CubeSat: a soft x-ray sky monitor, transient finder, and burst detector for high-energy and multimessenger astophysics," in *Space Telescopes and Instrumentation 2018: Ultraviolet to Gamma Ray*, J.-W. A. den Herder, S. Nikzad, and K. Nakazawa, Eds., *Society of Photo-Optical Instrumentation Engineers (SPIE) Conference Series* **10699**, 106995S (2018).

8 S. Zheng, "The status of GECAM mission," in *The Extragalactic Explosive Universe: the New Era of Transient Surveys and Data-Driven Discovery*, 63 (2019).

9 J. Wen, X. Long, X. Zheng, *et al.*, "GRID: a student project to monitor the transient gamma-ray sky in the multi-messenger astronomy era," *Experimental Astronomy* **48**, 77–95 (2019).

10 J. E. Grove, C. C. Cheung, M. Kerr, *et al.*, "Glowbug, a Low-Cost, High-Sensitivity Gamma-Ray Burst Telescope," in *Gamma-ray Bursts in the Gravitational Wave Era 2019*, 57–59 (2020).

11 F. Fuschino, R. Campana, C. Labanti, *et al.*, "HERMES: An ultra-wide band X and gamma-ray transient monitor on board a nano-satellite constellation," *Nuclear Instruments and Methods in Physics Research A* **936**, 199–203 (2019).

12 M. Pearce, L. Eliasson, N. Kumar Iyer, *et al.*, "Science prospects for SPHiNX - A small satellite GRB polarimetry mission," *Astroparticle Physics* **104**, 54–63 (2019).

13 J. Řípa, G. Galgóczi, N. Werner, *et al.*, "Estimation of the detected background by the future gamma ray transient mission CAMELOT," *Astronomische Nachrichten* **340**, 666–673 (2019).

14 Z. Bagoly, L. G. Balázs, G. Galgóczi, *et al.*, "Transient detection capabilities of small satellite gamma-ray detectors," *Astronomische Nachrichten* **340**, 681–689 (2019).

15 G. Vedrenne and J.-L. Atteia, *Gamma-Ray Bursts: The brightest explosions in the Universe*, Springer, Berlin (2009).

16 C. Kouveliotou, R. A. M. J. Wijers, and S. Woosley, *Gamma-ray Bursts*, Cambridge University Press, Cambridge (2012).

17 A. Levan, *Gamma-Ray Bursts*, IOP Publishing, Bristol (2018).

18 B. Zhang, *The Physics of Gamma-Ray Bursts*, Cambridge University Press, Cambridge (2019).

19 C. Kouveliotou, C. A. Meegan, G. J. Fishman, *et al.*, "Identification of two classes of gamma-ray bursts," *The Astrophysical Journal* **413**, L101–L104 (1993).

20 S. Mereghetti, "The strongest cosmic magnets: soft gamma-ray repeaters and anomalous X-ray pulsars," *The Astronomy and Astrophysics Review* **15**, 225–287 (2008).

21 K. Yamaoka, M. Ohno, M. S. Tashiro, *et al.*, "Suzaku Wide-band All-sky Monitor (WAM) observations of GRBs and SGRs," *Publications of the Astronomical Society of Japan* **69**, R2 (2017).

22 A. Lindanger, M. Marisaldi, C. Maiorana, *et al.*, "The 3rd agile terrestrial gamma ray flash catalog. part i: Association to lightning sferics," *Journal of Geophysical Research: Atmospheres* , e2019JD031985 (2020).

23 J. R. Dwyer, D. M. Smith, and S. A. Cummer, "High-Energy Atmospheric Physics: Terrestrial Gamma-Ray Flashes and Related Phenomena," *Space Science Reviews* **173**, 133–196 (2012).

24 D. Gruber, A. Goldstein, V. Weller von Ahlefeld, *et al.*, "The fermi gbm gamma-ray burst spectral catalog: Four years of data," *The Astrophysical Journal Supplement* **211**(1), 12 (2014).

25 A. von Kienlin, C. A. Meegan, W. S. Paciesas, *et al.*, "The Second Fermi GBM Gamma-Ray Burst Catalog: The First Four Years," *The Astrophysical Journal Supplement* **211**(1), 13 (2014).

26 P. Narayana Bhat, C. A. Meegan, A. von Kienlin, *et al.*, "The Third Fermi GBM Gamma-Ray Burst Catalog: The First Six Years," *The Astrophysical Journal Supplement* **223**(2), 28 (2016).

27 A. von Kienlin, C. A. Meegan, W. S. Paciesas, *et al.*, "The Fourth Fermi-GBM Gamma-Ray Burst Catalog: A Decade of Data," *The Astrophysical Journal* **893**, 46 (2020).

28 A. Goldstein, E. Burns, R. Hamburg, *et al.*, "Updates to the Fermi-GBM Short GRB Targeted Offline Search in Preparation for LIGO's Second Observing Run," *arXiv e-prints* , arXiv:1612.02395 (2016).

29 R. C. Duncan and C. Thompson, "Formation of Very Strongly Magnetized Neutron Stars: Implications for Gamma-Ray Bursts," *The Astrophysical Journal Letters* **392**, L9 (1992).

30 C. Thompson and R. C. Duncan, "The soft gamma repeaters as very strongly magnetized neutron stars - I. Radiative mechanism for outbursts," *Monthly Notices of the Royal Astronomical Society* **275**, 255–300 (1995).

31 C. Thompson and R. C. Duncan, "The Soft Gamma Repeaters as Very Strongly Magnetized Neutron Stars. II. Quiescent Neutrino, X-Ray, and Alfven Wave Emission," *The Astrophysical Journal* **473**, 322 (1996).

32 W. H. G. Lewin and M. van der Klis, *Compact Stellar X-ray Sources*, Cambridge University Press, Cambridge, UK (2006).

33 V. M. Kaspi, "Recent progress on anomalous X-ray pulsars," *Astrophysics and Space Science* **308**, 1–11 (2007).

34 T. Enoto, S. Kisaka, and S. Shibata, "Observational diversity of magnetized neutron stars," *Reports on Progress in Physics* **82**, 106901 (2019).

35 E. P. Mazets, S. V. Golentskii, V. N. Ilinskii, *et al.*, "Observations of a flaring X-ray pulsar in Dorado," *Nature* **282**, 587–589 (1979).

36 C. Kouveliotou, S. Dieters, T. Strohmayer, *et al.*, "An X-ray pulsar with a superstrong magnetic field in the soft γ-ray repeater SGR1806 - 20," *Nature* **393**, 235–237 (1998).

37 S. Mereghetti, D. Götz, I. F. Mirabel, *et al.*, "INTEGRAL discovery of persistent hard X-ray emission from the Soft Gamma-ray Repeater SGR 1806-20," *Astronomy and Astrophysics* **433**, L9–L12 (2005).

38 S. Molkov, K. Hurley, R. Sunyaev, *et al.*, "The broad-band spectrum of the persistent emission from SGR 1806-20," *Astronomy and Astrophysics* **433**, L13–L16 (2005).

39 K. Hurley, S. E. Boggs, D. M. Smith, *et al.*, "An exceptionally bright flare from SGR 1806-20 and the origins of short-duration γ-ray bursts," *Nature* **434**, 1098–1103 (2005).

40 E. P. Mazets, T. L. Cline, R. L. Aptekar, *et al.*, "The Konus-Wind and Helicon-Coronas-F

detection of the giant γ-ray flare from the soft γ-ray repeater SGR 1806-20," *arXiv e-prints*
, astro–ph/0502541 (2005).

41 S. Mereghetti, D. Götz, A. von Kienlin, *et al.*, "The First Giant Flare from SGR 1806-20: Observations Using the Anticoincidence Shield of the Spectrometer on INTEGRAL," *The Astrophysical Journal Letters* **624**, L105–L108 (2005).

42 D. M. Palmer, S. Barthelmy, N. Gehrels, *et al.*, "A giant γ-ray flare from the magnetar SGR 1806 - 20," *Nature* **434**, 1107–1109 (2005).

43 T. Terasawa, Y. T. Tanaka, Y. Takei, *et al.*, "Repeated injections of energy in the first 600ms of the giant flare of SGR1806 - 20," *Nature* **434**, 1110–1111 (2005).

44 R. L. Aptekar, D. D. Frederiks, S. V. Golenetskii, *et al.*, "Konus Catalog of Soft Gamma Repeater Activity: 1978 to 2000," *The Astrophysical Journal Supplement* **137**, 227–277 (2001).

45 G. J. Fishman, P. N. Bhat, R. Mallozzi, *et al.*, "Discovery of Intense Gamma-Ray Flashes of Atmospheric Origin," *Science* **264**, 1313–1316 (1994).

46 D. M. Smith, L. I. Lopez, R. P. Lin, *et al.*, "Terrestrial Gamma-Ray Flashes Observed up to 20 MeV," *Science* **307**, 1085–1088 (2005).

47 B. W. Grefenstette, D. M. Smith, B. J. Hazelton, *et al.*, "First RHESSI terrestrial gamma ray flash catalog," *Journal of Geophysical Research (Space Physics)* **114**, A02314 (2009).

48 M. S. Briggs, G. J. Fishman, V. Connaughton, *et al.*, "First results on terrestrial gamma ray flashes from the Fermi Gamma-ray Burst Monitor," *Journal of Geophysical Research (Space Physics)* **115**, A07323 (2010).

49 G. J. Fishman, M. S. Briggs, V. Connaughton, *et al.*, "Temporal properties of the terrestrial gamma-ray flashes from the Gamma-Ray Burst Monitor on the Fermi Observatory," *Journal of Geophysical Research (Space Physics)* **116**, A07304 (2011).

50 O. J. Roberts, G. Fitzpatrick, M. Stanbro, *et al.*, "The First Fermi-GBM Terrestrial Gamma Ray Flash Catalog," *Journal of Geophysical Research (Space Physics)* **123**, 4381–4401 (2018).

51 M. Marisaldi, F. Fuschino, C. Labanti, *et al.*, "AGILE Observations of Terrestrial Gamma-Ray Flashes," *2011 Fermi Symposium proceedings - eConf C110509* , arXiv:1111.2188 (2011).

52 M. Marisaldi, F. Fuschino, M. Tavani, *et al.*, "Properties of terrestrial gamma ray flashes detected by AGILE MCAL below 30 MeV," *Journal of Geophysical Research (Space Physics)* **119**, 1337–1355 (2014).

53 M. Marisaldi, A. Argan, A. Ursi, *et al.*, "Enhanced detection of terrestrial gamma-ray flashes by AGILE," *Geophysical Research Letters* **42**, 9481–9487 (2015).

54 C. Labanti, M. Marisaldi, F. Fuschino, *et al.*, "Design and construction of the Mini-Calorimeter of the AGILE satellite," *Nuclear Instruments and Methods in Physics Research A* **598**, 470–479 (2009).

55 C. Maiorana, M. Marisaldi, A. Lindanger, *et al.*, "The 3rd agile terrestrial gamma-ray flashes catalog. part ii: Optimized selection criteria and characteristics of the new sample," *Journal of Geophysical Research: Atmospheres* , e2019JD031986 (2020).

56 M. Marisaldi, M. Galli, C. Labanti, *et al.*, "On the high-energy spectral component and fine

time structure of terrestrial gamma ray flashes," *Journal of Geophysical Research: Atmospheres* **124**, 7484–7497 (2019).

57 D. Tierney, M. S. Briggs, G. Fitzpatrick, *et al.*, "Fluence distribution of terrestrial gamma ray flashes observed by the Fermi Gamma-ray Burst Monitor," *Journal of Geophysical Research (Space Physics)* **118**, 6644–6650 (2013).

58 A. S. Jursa, *Handbook of geophysics and the space environment*, Air Force Geophysics Laboratory, Air Force Systems Command, United States Air Force, Springfield, USA (1985).

59 T. W. Armstrong and B. L. Colborn, "Predictions of induced radioactivity for spacecraft in low Earth orbit," *International Journal of Radiation Applications and Instrumentation. Part D. Nuclear Tracks and Radiation Measurements* **20**(1), 101–130 (1992). Special Issue Space Radiation.

60 N. Gehrels, "Instrumental background in gamma-ray spectrometers flown in low earth orbit," *Nuclear Instruments and Methods in Physics Research, Section A* **313**, 513–528 (1992).

61 A. J. Dean, A. J. Bird, N. Diallo, *et al.*, "The Modelling of Background Noise in Astronomical Gamma Ray Telescopes," *Space Science Reviews* **105**, 285–376 (2003).

62 J. L. Barth, C. S. Dyer, and E. G. Stassinopoulos, "Space, atmospheric, and terrestrial radiation environments," *IEEE Transactions on Nuclear Science* **50**, 466–482 (2003).

63 T. Mizuno, T. Kamae, G. Godfrey, *et al.*, "Cosmic-Ray Background Flux Model Based on a Gamma-Ray Large Area Space Telescope Balloon Flight Engineering Model," *The Astrophysical Journal* **614**, 1113–1123 (2004).

64 M. Zombeck, *Handbook of Space Astronomy and Astrophysics: Third Edition*, Cambridge University Press, Cambridge, UK (2007).

65 V. Fioretti, A. Bulgarelli, G. Malaguti, *et al.*, "The low Earth orbit radiation environment and its impact on the prompt background of hard x-ray focusing telescopes," in *Proceedings of the SPIE*, *Society of Photo-Optical Instrumentation Engineers (SPIE) Conference Series* **8453**, 845331 (2012).

66 R. Campana, M. Feroci, E. Del Monte, *et al.*, "Background simulations for the Large Area Detector onboard LOFT," *Experimental Astronomy* **36**, 451–477 (2013).

67 M. A. Xapsos, P. M. O'Neill, and T. P. O'Brien, "Near-Earth Space Radiation Models," *IEEE Transactions on Nuclear Science* **60**, 1691–1705 (2013).

68 B. Zabori, A. Hirn, J. Eastwood, *et al.*, "Space radiation and magnetic field environment specification for the radcube space weather related cubesat mission," in *69th International Astronautical Congress*, IAC–18,A1,5,2,x42514 (2018).

69 P. Cumani, M. Hernanz, J. Kiener, *et al.*, "Background for a gamma-ray satellite on a low-Earth orbit," *Experimental Astronomy* **47**, 273–302 (2019).

70 S. Mate, L. Bouchet, J.-L. Atteia, *et al.*, "Simulations of the SVOM/ECLAIRs dynamic background: a fast, accurate and general approach for wide-field hard X-ray instruments," *Experimental Astronomy* **48**, 171–198 (2019).

71 ESA, "Space engineering - Space environment," Tech. Rep. ECSS-E-ST-10-04C, ESA Requirements and Standards Division (2008).

72 J. F. Ormes, T. Burnett, E. Grove, *et al.*, "GLAST LAT Background Review," Tech. Rep. LAT-TD-08316-01, NASA (2006).

73 R. Giacconi, H. Gursky, F. R. Paolini, *et al.*, "Evidence for x Rays From Sources Outside the Solar System," *Physical Review Letters* **9**, 439–443 (1962).

74 K. Kasturirangan and U. R. Rao, "Spectrum of the Cosmic X- and Gamma Ray Background in the Energy Range 1 keV-1 MeV," *Astrophysics and Space Science* **15**, 161–166 (1972).

75 D. A. Schwartz and L. E. Peterson, "The Spectrum of Diffuse Cosmic X-Rays Observed by OSO-3 Between 7 and 100 KEV," *The Astrophysical Journal* **190**, 297–304 (1974).

76 V. Schoenfelder, U. Graser, and J. Daugherty, "Diffuse cosmic and atmospheric MeV gamma radiation from balloon observations.," *The Astrophysical Journal* **217**, 306–319 (1977).

77 C. E. Fichtel, G. A. Simpson, and D. J. Thompson, "Diffuse gamma radiation.," *The Astrophysical Journal* **222**, 833–849 (1978).

78 V. Schoenfelder, F. Graml, and F. P. Penningsfeld, "The vertical component of 1-20 MeV gamma rays at balloon altitudes," *The Astrophysical Journal* **240**, 350–362 (1980).

79 E. Boldt, "The Cosmic X-Ray Background," *Comments on Astrophysics* **9**, 97 (1981).

80 H. M. Horstman, G. Cavallo, and E. Moretti-Horstman, "The X and gamma diffuse background.," *Nuovo Cimento Rivista Serie* **5**, 255–311 (1975).

81 P. Sreekumar, D. L. Bertsch, B. L. Dingus, *et al.*, "EGRET Observations of the Extragalactic Gamma-Ray Emission," *The Astrophysical Journal* **494**, 523–534 (1998).

82 E. Churazov, R. Sunyaev, M. Revnivtsev, *et al.*, "INTEGRAL observations of the cosmic X-ray background in the 5-100 keV range via occultation by the Earth," *Astronomy and Astrophysics* **467**, 529–540 (2007).

83 F. Frontera, M. Orlandini, R. Landi, *et al.*, "The Cosmic X-Ray Background and the Population of the Most Heavily Obscured AGNs," *The Astrophysical Journal* **666**, 86–95 (2007).

84 M. Ajello, J. Greiner, G. Sato, *et al.*, "Cosmic X-Ray Background and Earth Albedo Spectra with Swift BAT," *The Astrophysical Journal* **689**, 666–677 (2008).

85 M. Ajello, L. Costamante, R. M. Sambruna, *et al.*, "The Evolution of Swift/BAT Blazars and the Origin of the MeV Background," *The Astrophysical Journal* **699**, 603–625 (2009).

86 A. Moretti, C. Pagani, G. Cusumano, *et al.*, "A new measurement of the cosmic X-ray background," *Astronomy and Astrophysics* **493**, 501–509 (2009).

87 M. Türler, M. Chernyakova, T. J. L. Courvoisier, *et al.*, "INTEGRAL hard X-ray spectra of the cosmic X-ray background and Galactic ridge emission," *Astronomy and Astrophysics* **512**, A49 (2010).

88 M. Ackermann, M. Ajello, A. Albert, *et al.*, "The Spectrum of Isotropic Diffuse Gamma-Ray Emission between 100 MeV and 820 GeV," *The Astrophysical Journal* **799**, 86 (2015).

89 Z. Bagoly, A. Meszaros, and P. Meszaros, "Cosmological Constraints on the Clustering of X-Ray Background Sources," *The Astrophysical Journal* **333**, 54 (1988).

90 A. Meszaros and P. Meszaros, "Large-Scale Structure of the Universe: Constraints from the X-Ray Background," *The Astrophysical Journal* **327**, 25 (1988).

91 H. G. Bi, A. Meszaros, and P. Meszaros, "On the large scale structure of X-ray background sources," *Astronomy and Astrophysics* **243**, 16–22 (1991).

92 K. Jahoda, O. Lahav, R. F. Mushotzky, *et al.*, "Cross-Correlation of the X-Ray Background with Nearby Galaxies," *The Astrophysical Journal* **378**, L37 (1991).

93 T. Shanks, I. Georgantopoulos, G. C. Stewart, *et al.*, "The origin of the cosmic X-ray background," *Nature* **353**, 315–320 (1991).

94 A. C. Fabian and X. Barcons, "The origin of the X-ray background.," *Annual Review of Astron and Astrophys* **30**, 429–456 (1992).

95 A. Comastri, G. Setti, G. Zamorani, *et al.*, "The contribution of AGNs to the X-ray background.," *Astronomy and Astrophysics* **296**, 1 (1995).

96 A. A. Zdziarski, "Contributions of AGNs and SNe IA to the cosmic X-ray and gamma-ray backgrounds," *Monthly Notices of the Royal Astronomical Society* **281**, L9 (1996).

97 W. N. Brandt and G. Hasinger, "Deep Extragalactic X-Ray Surveys," *Annual Review of Astron and Astrophys* **43**, 827–859 (2005).

98 N. Cappelluti, P. Ranalli, M. Roncarelli, *et al.*, "The nature of the unresolved extragalactic cosmic soft X-ray background," *Monthly Notices of the Royal Astronomical Society* **427**, 651–663 (2012).

99 K. Helgason, N. Cappelluti, G. Hasinger, *et al.*, "The Contribution of z <~6 Sources to the Spatial Coherence in the Unresolved Cosmic Near-infrared and X-Ray Backgrounds," *The Astrophysical Journal* **785**, 38 (2014).

100 N. Cappelluti, Y. Li, A. Ricarte, *et al.*, "The Chandra COSMOS Legacy Survey: Energy Spectrum of the Cosmic X-Ray Background and Constraints on Undetected Populations," *The Astrophysical Journal* **837**, 19 (2017).

101 Q. Ma, B. Ciardi, M. B. Eide, *et al.*, "X-ray background and its correlation with the 21 cm signal," *Monthly Notices of the Royal Astronomical Society* **480**, 26–34 (2018).

102 A. A. Penzias and R. W. Wilson, "A Measurement of Excess Antenna Temperature at 4080 Mc/s.," *The Astrophysical Journal* **142**, 419–421 (1965).

103 I. V. Moskalenko and A. W. Strong, "Anisotropic Inverse Compton Scattering in the Galaxy," *The Astrophysical Journal* **528**, 357–367 (2000).

104 A. Dar and A. De Rújula, "Is the diffuse gamma background radiation generated by Galactic cosmic rays?," *Monthly Notices of the Royal Astronomical Society* **323**, 391–401 (2001).

105 D. E. Gruber, J. L. Matteson, L. E. Peterson, *et al.*, "The Spectrum of Diffuse Cosmic Hard X-Rays Measured with HEAO 1," *The Astrophysical Journal* **520**, 124–129 (1999).

106 R. Rothschild, E. Boldt, S. Holt, *et al.*, "The cosmic X-ray experiment aboard HEAO-1.," *Space Science Instrumentation* **4**, 269–301 (1979).

107 N. Gehrels, E. Chipman, and D. A. Kniffen, "The Compton Gamma Ray Observatory.," *Astronomy and Astrophysics Supplement Series* **97**, 5–12 (1993).

108 F. Melia, *High-Energy Astrophysics*, Princeton University Press, New Jersey (2009).

109 V. Schönfelder, *The Universe in Gamma Rays*, Springer, Berlin (2001).

110 A. W. Strong, I. V. Moskalenko, and O. Reimer, "Diffuse Continuum Gamma Rays from the Galaxy," *The Astrophysical Journal* **537**, 763–784 (2000).

111 C. E. Fichtel, R. C. Hartman, D. A. Kniffen, *et al.*, "High-energy gamma-ray results from the second Small Astronomy Satellite.," *The Astrophysical Journal* **198**, 163–182 (1975).

112 C. E. Fichtel, R. C. Hartman, D. A. Kniffen, *et al.*, "Tabulated data from the SAS-2 high energy gamma ray telescope," Tech. Rep. NASA-TM-79650, NASA Goddard Space Flight Center (1978).

113 D. L. Bertsch, T. M. Dame, C. E. Fichtel, *et al.*, "Diffuse Gamma-Ray Emission in the Galactic Plane from Cosmic-Ray, Matter, and Photon Interactions," *The Astrophysical Journal* **416**, 587 (1993).

114 W. L. Kraushaar, G. W. Clark, G. P. Garmire, *et al.*, "High-Energy Cosmic Gamma-Ray Observations from the OSO-3 Satellite," *The Astrophysical Journal* **177**, 341 (1972).

115 H. A. Mayer-Hasselwander, K. Bennett, G. F. Bignami, *et al.*, "Large-scale distribution of galactic gamma radiation observed by COS-B," *Astronomy and Astrophysics* **105**, 164–175 (1982).

116 R. Krivonos, M. Revnivtsev, E. Churazov, *et al.*, "Hard X-ray emission from the Galactic ridge," *Astronomy and Astrophysics* **463**, 957–967 (2007).

117 T. A. Porter, I. V. Moskalenko, A. W. Strong, *et al.*, "Inverse Compton Origin of the Hard X-Ray and Soft Gamma-Ray Emission from the Galactic Ridge," *The Astrophysical Journal* **682**, 400–407 (2008).

118 L. Bouchet, E. Jourdain, J. P. Roques, *et al.*, "INTEGRAL SPI All-Sky View in Soft Gamma Rays: A Study of Point-Source and Galactic Diffuse Emission," *The Astrophysical Journal* **679**, 1315–1326 (2008).

119 R. Krivonos, M. Revnivtsev, S. Tsygankov, *et al.*, "INTEGRAL/IBIS 7-year All-Sky Hard X-ray Survey. I. Image reconstruction," *Astronomy and Astrophysics* **519**, A107 (2010).

120 R. Krivonos, S. Tsygankov, A. Lutovinov, *et al.*, "INTEGRAL 11-year hard X-ray survey above 100 keV," *Monthly Notices of the Royal Astronomical Society* **448**, 3766–3774 (2015).

121 S. D. Hunter, D. L. Bertsch, J. R. Catelli, *et al.*, "EGRET Observations of the Diffuse Gamma-Ray Emission from the Galactic Plane," *The Astrophysical Journal* **481**, 205–240 (1997).

122 A. W. Strong, H. Bloemen, R. Diehl, *et al.*, "COMPTEL Skymapping: a New Approach Using Parallel Computing," *Astrophysical Letters and Communications* **39**, 209 (1999).

123 A. W. Strong, I. V. Moskalenko, and O. Reimer, "Diffuse Galactic Continuum Gamma Rays: A Model Compatible with EGRET Data and Cosmic-Ray Measurements," *The Astrophysical Journal* **613**, 962–976 (2004).

124 N. Prantzos, C. Boehm, A. M. Bykov, *et al.*, "The 511 keV emission from positron annihilation in the Galaxy," *Reviews of Modern Physics* **83**, 1001–1056 (2011).

125 A. W. Strong, "Interstellar Gamma Rays and Cosmic Rays:. New Insights from Fermi-Lat and Integral," in *Cosmic Rays for Particle and Astroparticle Physics*, S. Giani, C. Leroy, and P. G. Rancoita, Eds., 473–481, Scientific Publishing Co. Pte. Ltd. (Singapore) (2011).

126 A. A. Abdo, M. Ackermann, M. Ajello, *et al.*, "Spectrum of the Isotropic Diffuse Gamma-Ray Emission Derived from First-Year Fermi Large Area Telescope Data," *Physical Review Letters* **104**, 101101 (2010).

127 M. Ajello, A. Albert, W. B. Atwood, *et al.*, "Fermi-LAT Observations of High-Energy Gamma-Ray Emission toward the Galactic Center," *The Astrophysical Journal* **819**, 44 (2016).

128 M. Revnivtsev, S. Sazonov, M. Gilfanov, *et al.*, "Origin of the Galactic ridge X-ray emission," *Astronomy and Astrophysics* **452**, 169–178 (2006).

129 K. Oh, M. Koss, C. B. Markwardt, *et al.*, "The 105-Month Swift-BAT All-sky Hard X-Ray Survey," *The Astrophysical Journals Supplement* **235**, 4 (2018).

130 J. A. van Allen, "Observation of high intensity radiation by satellites 1958 alpha and gamma," *Journal of Jet Propulsion* **28**(9), 588–592 (1958).

131 S. I. Svertilov, M. I. Panasyuk, V. V. Bogomolov, *et al.*, "Wide-Field Gamma-Spectrometer BDRG: GRB Monitor On-Board the Lomonosov Mission," *Space Science Reviews* **214**, 8 (2018).

132 M. I. Panasyuk, V. M. Lipunov, I. Pack, *et al.*, "Complete set of detectors for studying cosmic gamma-ray bursts onboard the Lomonosov satellite," *Physics of Particles and Nuclei* **49**, 109–112 (2018).

133 J. G. Roederer, *Dynamics of geomagnetically trapped radiation*, Springer-Verlag, New York, USA (1970).

134 M. G. Kivelson and C. T. Russell, *Introduction to Space Physics*, Cambridge University Press, Cambridge, UK (1995).

135 M. Walt, *Introduction to Geomagnetically Trapped Radiation*, Cambridge University Press, Cambridge, UK (2005).

136 M. Qin, X. Zhang, B. Ni, *et al.*, "Solar cycle variations of trapped proton flux in the inner radiation belt," *Journal of Geophysical Research (Space Physics)* **119**, 9658–9669 (2014).

137 O. Adriani, G. C. Barbarino, G. A. Bazilevskaya, *et al.*, "Trapped Proton Fluxes at Low Earth Orbits Measured by the PAMELA Experiment," *The Astrophysical Journal* **799**, L4 (2015).

138 V. V. Benghin, O. Y. Nechaev, I. A. Zolotarev, *et al.*, "An Experiment in Radiation Measurement Using the Depron Instrument," *Space Science Reviews* **214**, 9 (2018).

139 Y. Y. Shprits, V. Angelopoulos, C. T. Russell, *et al.*, "Scientific Objectives of Electron Losses and Fields INvestigation Onboard Lomonosov Satellite," *Space Science Reviews* **214**, 25 (2018).

140 J. I. Vette, "The AE-8 trapped electron model environment," Tech. Rep. NSSDC/WDC-A-R&S 91-24, The NASA/National Space Science Data Center (1991a).

141 J. I. Vette, "Trapped Radiation Environment Model Program (1964-1991)," Tech. Rep. NSSDC/WDC-A-R&S 91-29, The NASA/National Space Science Data Center (1991b).

142 D. M. Sawyer and J. I. Vette, "Trapped Proton Environment for Solar Maximum and Solar Minimum," Tech. Rep. NSSDC/WDC-A-R&S 76-06, The NASA/National Space Science Data Center (1976).

143 A. L. Vampola, "The ESA Outer Zone Electron Model Update," in *Environment Modeling for Space-Based Applications*, T. D. Guyenne and A. Hilgers, Eds., *ESA Special Publication* **392**, 151 (1996).

144 D. Heynderickx, M. Kruglanski, V. Pierrard, *et al.*, "A low altitude trapped proton model for solar minimum conditions based on SAMPEX/PET data," *IEEE Transactions on Nuclear Science* **46**, 1475–1480 (1999).

145 G. P. Ginet, T. P. O'Brien, S. L. Huston, *et al.*, "AE9, AP9 and SPM: New Models for Specifying the Trapped Energetic Particle and Space Plasma Environment," *Space Science Reviews* **179**, 579–615 (2013).

146 W. R. Johnston, T. P. O'Brien, G. P. Ginet, *et al.*, "AE9/AP9/SPM: new models for radiation belt and space plasma specification," in *Proceedings of the SPIE*, *Society of Photo-Optical Instrumentation Engineers (SPIE) Conference Series* **9085**, 908508 (2014).

147 W. R. Johnston, T. P. O'Brien, S. L. Huston, *et al.*, "Recent Updates to the AE9/AP9/SPM Radiation Belt and Space Plasma Specification Model," *IEEE Transactions on Nuclear Science* **62**, 2760–2766 (2015).

148 T. P. O'Brien, W. R. Johnston, S. L. Huston, *et al.*, "Changes in AE9/AP9-IRENE Version 1.5," *IEEE Transactions on Nuclear Science* **65**, 462–466 (2018).

149 M. de Soria-Santacruz Pich, I. Jun, and R. Evans, "Empirical radiation belt models: Comparison with in situ data and implications for environment definition," *Space Weather* **15**, 1165–1176 (2017).

150 J. Řípa, G. Dilillo, R. Campana, *et al.*, "A comparison of trapped particle models in low Earth orbit," in *Space Telescopes and Instrumentation 2020: Ultraviolet to Gamma Ray*, J.-W. A. den Herder, S. Nikzad, and K. Nakazawa, Eds., **11444**, 114443P, International Society for Optics and Photonics, SPIE (2020).

151 G. P. Ginet, B. K. Dichter, D. H. Brautigam, *et al.*, "Proton Flux Anisotropy in Low Earth Orbit," *IEEE Transactions on Nuclear Science* **54**, 1975–1980 (2007).

152 J. Alcaraz, D. Alvisi, B. Alpat, *et al.*, "Protons in near earth orbit," *Physics Letters B* **472**, 215–226 (2000).

153 J. Alcaraz, B. Alpat, G. Ambrosi, *et al.*, "Leptons in near earth orbit," *Physics Letters B* **484**, 10–22 (2000).

154 T. Sanuki, M. Motoki, H. Matsumoto, *et al.*, "Precise Measurement of Cosmic-Ray Proton and Helium Spectra with the BESS Spectrometer," *The Astrophysical Journal* **545**, 1135–1142 (2000).

155 Y. S. Yoon, H. S. Ahn, P. S. Allison, *et al.*, "Cosmic-ray Proton and Helium Spectra from the First CREAM Flight," *The Astrophysical Journal* **728**, 122 (2011).

156 M. Ackermann, M. Ajello, W. B. Atwood, *et al.*, "Fermi LAT observations of cosmic-ray electrons from 7 GeV to 1 TeV," *Physical Review D* **82**, 092004 (2010).

157 M. Ackermann, M. Ajello, A. Albert, *et al.*, "Inferred Cosmic-Ray Spectrum from Fermi Large Area Telescope γ-Ray Observations of Earth's Limb," *Physical Review Letters* **112**, 151103 (2014).

158 F. Aharonian, A. G. Akhperjanian, U. Barres de Almeida, *et al.*, "Energy Spectrum of Cosmic-Ray Electrons at TeV Energies," *Physical Review Letters* **101**, 261104 (2008).

159 M. Martucci, R. Munini, M. Boezio, *et al.*, "Proton Fluxes Measured by the PAMELA Experiment from the Minimum to the Maximum Solar Activity for Solar Cycle 24," *The Astrophysical Journal Letters* **854**, L2 (2018).

160 "Space environment (natural and artificial) - Galactic cosmic ray model," Tech. Rep. ISO-15390, International Organization for Standardization (2004).

161 D. F. Smart and M. A. Shea, "A review of geomagnetic cutoff rigidities for earth-orbiting spacecraft," *Advances in Space Research* **36**, 2012–2020 (2005).

162 T. E. VanZandt, W. L. Clark, and J. M. Warnock, "Magnetic apex coordinates: A magnetic coordinate system for the ionospheric F $_2$ layer," *Journal of Geophysical Research* **77**, 2406 (1972).

163 W. R. Webber, "Cosmic ray electrons and positrons - A review of current measurements and some implications," in *NATO Advanced Science Institutes (ASI) Series C*, M. M. Shapiro, Ed., *NATO Advanced Science Institutes (ASI) Series C* **107**, 83–100 (1983).

164 I. V. Moskalenko and A. W. Strong, "Production and Propagation of Cosmic-Ray Positrons and Electrons," *The Astrophysical Journal* **493**, 694–707 (1998).

165 R. L. Golden, C. Grimani, B. L. Kimbell, *et al.*, "Observations of Cosmic-Ray Electrons and Positrons Using an Imaging Calorimeter," *The Astrophysical Journal* **436**, 769 (1994).

166 V. Bidoli, M. Casolino, M. de Pascale, *et al.*, "Energy spectrum of secondary protons above the atmosphere measured by the instruments nina and nina-2," *Annales Geophysicae* **20**(10), 1693 (2002).

167 C. E. McIlwain, "Coordinates for Mapping the Distribution of Magnetically Trapped Particles," *Journal of Geophysical Research* **66**, 3681–3691 (1961).

168 W. B. Atwood, A. A. Abdo, M. Ackermann, *et al.*, "The Large Area Telescope on the Fermi Gamma-Ray Space Telescope Mission," *The Astrophysical Journal* **697**(2), 1071 (2009).

169 P. Zuccon, B. Bertucci, B. Alpat, *et al.*, "A calculation of the radiation environment for satellite experiments operating below the van allen belts," in *Proceedings of the 28th International Cosmic Ray Conference*, **7**, 4249 (2003).

170 S. A. Voronov, A. M. Gal'Per, S. V. Koldashov, *et al.*, "Energy spectra of high-energy electrons and positrons under the earth's radiation belt," *Kosmicheskie Issledovaniia* **29**, 567 (1991).

171 V. V. Mikhailov, "Low Energy Electron and Positron Spectra in the Earth Orbit Measured by Maria-2 Instrument," *International Journal of Modern Physics A* **17**, 1695–1704 (2002).

172 D. J. Thompson, "A three-dimensional study of 30- to 300-MeV atmospheric gamma rays," *Journal of Geophysical Research* **79**, 1309–1320 (1974).

173 I. A. Gurian, E. P. Mazets, M. P. Proskura, *et al.*, "Investigation of hard gamma radiation of the atmosphere on Cosmos 461.," *Geomagnetism and Aeronomy* **19**, 11–17 (1979).

174 J. M. Ryan, M. C. Jennings, M. D. Radwin, *et al.*, "Atmospheric gamma ray angle and energy distributions from sea level to 3.5 g/cm^2 and 2 to 25 MeV," *Journal of Geophysical Research* **84**, 5279–5288 (1979).

175 A. Akyüz, D. Bhattacharya, K. W. Chuang, *et al.*, "Atmospheric gamma rays at geomagnetic latitudes of -29° and +43°," *Journal of Geophysical Research* **102**, 17,359–17,364 (1997).

176 D. Petry, "The Earth's Gamma-ray Albedo as observed by EGRET," in *High Energy Gamma-Ray Astronomy*, F. A. Aharonian, H. J. Völk, and D. Horns, Eds., *American Institute of Physics Conference Series* **745**, 709–714 (2005).

177 A. A. Abdo, M. Ackermann, M. Ajello, *et al.*, "Fermi large area telescope observations of the cosmic-ray induced γ-ray emission of the Earth's atmosphere," *Physical Review D* **80**, 122004 (2009).

178 W. L. Imhof, G. H. Nakano, and J. B. Reagan, "High-Resolution Measurements of Atmospheric Gamma Rays from a Satellite," *Journal of Geophysical Research* **81**, 2835 (1976).

179 S. Sazonov, E. Churazov, R. Sunyaev, *et al.*, "Hard X-ray emission of the Earth's atmosphere: Monte Carlo simulations," *Monthly Notices of the Royal Astronomical Society* **377**, 1726–1736 (2007).

180 D. J. Thompson, G. A. Simpson, and M. E. Ozel, "SAS 2 Observations of the Earth Albedo Gamma Radiation Above 35 MeV," *Journal of Geophysical Research* **86**, 1265–1270 (1981).

181 F. Ait-Ouamer, A. D. Zych, and R. S. White, "Atmospheric neutrons at 8.5-GV cutoff in the southern hemisphere," *Journal of Geophysical Research* **93**, 2499–2510 (1988).

182 D. J. Morris, H. Aarts, K. Bennett, *et al.*, "Neutron measurements in near-Earth orbit with COMPTEL," *Journal of Geophysical Research* **100**, 12243–12250 (1995).

183 F. Lei, S. Clucas, C. Dyer, *et al.*, "An Atmospheric Radiation Model Based on Response Ma-

trices Generated by Detailed Monte Carlo Simulations of Cosmic Ray Interactions," *IEEE Transactions on Nuclear Science* **51**, 3442–3451 (2004).

184 F. Lei, A. Hands, S. Clucas, *et al.*, "Improvement to and Validations of the QinetiQ Atmospheric Radiation Model (QARM)," *IEEE Transactions on Nuclear Science* **53**, 1851–1858 (2006).

185 R. E. Lingenfelter, "The Cosmic-Ray Neutron Leakage Flux," *Journal of Geophysical Research* **68**, 5633 (1963).

186 M. Kole, M. Pearce, and M. Muñoz Salinas, "A model of the cosmic ray induced atmospheric neutron environment," *Astroparticle Physics* **62**, 230–240 (2015).

187 M. Ohno, N. Werner, A. Pál, *et al.*, "CAMELOT: design and performance verification of the detector concept and localization capability," in *Proceedings of the SPIE*, *Society of Photo-Optical Instrumentation Engineers (SPIE) Conference Series* **10699**, 1069964 (2018).

188 K. Torigoe, Y. Fukazawa, G. Galgóczi, *et al.*, "Performance study of a large CsI(Tl) scintillator with an MPPC readout for nanosatellites used to localize gamma-ray bursts," *Nuclear Instruments and Methods in Physics Research A* **924**, 316–320 (2019).

189 C. M. Poole, I. Cornelius, J. V. Trapp, *et al.*, "A CAD Interface for GEANT4," *Australasian Physical & Engineering Science in Medicine* **35**, 329–334 (2012).

190 J. D. Sullivan, "Geometrical factor and directional response of single and multi-element particle telescopes," *Nuclear Instruments and Methods* **95**, 5–11 (1971).

191 H. Si, "TetGen, a Delaunay-Based Quality Tetrahedral Mesh Generator," *ACM Trans. on Mathematical Software* **41**, 11 (2015).

192 M. Feroci, F. Frontera, E. Costa, *et al.*, "In-flight performances of the BeppoSAX gamma-ray burst monitor," in *EUV, X-Ray, and Gamma-Ray Instrumentation for Astronomy VIII*, O. H. Siegmund and M. A. Gummin, Eds., *Society of Photo-Optical Instrumentation Engineers (SPIE) Conference Series* **3114**, 186–197 (1997).

193 D. L. Band, "A Gamma-Ray Burst Trigger Tool Kit," *The Astrophysical Journal* **578**, 806–811 (2002).

194 E. E. Fenimore and M. Galassi, "The HETE Triggering Algorithm," in *Gamma-ray Bursts in the Afterglow Era*, E. Costa, F. Frontera, and J. Hjorth, Eds., *ESO Astrophysics Symposia*, 393, Springer-Verlag (2001).

195 E. E. Fenimore, D. Palmer, M. Galassi, *et al.*, "The Trigger Algorithm for the Burst Alert Telescope on Swift," in *Gamma-Ray Burst and Afterglow Astronomy 2001: A Workshop Celebrating the First Year of the HETE Mission*, G. R. Ricker and R. K. Vanderspek, Eds., *American Institute of Physics Conference Series* **662**, 491–493 (2003).

196 M. Feroci, E. Costa, P. Soffitta, *et al.*, "SuperAGILE: The hard X-ray imager for the AGILE space mission," *Nuclear Instruments and Methods in Physics Research A* **581**, 728–754 (2007).

197 F. Fuschino, C. Labanti, M. Galli, *et al.*, "Search of GRB with AGILE Minicalorimeter," *Nuclear Instruments and Methods in Physics Research A* **588**, 17–21 (2008).

198 D. M. Smith, R. P. Lin, P. Turin, *et al.*, "The RHESSI Spectrometer," *Solar Physics* **210**, 33–60 (2002).

199 G. Fitzpatrick, S. McBreen, V. Connaughton, *et al.*, "Background estimation in a wide-field background-limited instrument such as Fermi GBM," in *Space Telescopes and Instrumenta-*

tion 2012: Ultraviolet to Gamma Ray, T. Takahashi, S. S. Murray, and J.-W. A. den Herder, Eds., *Society of Photo-Optical Instrumentation Engineers (SPIE) Conference Series* **8443**, 84433B (2012).

200 M. Kokubun, Y. Fukazawa, E. Idesawa, *et al.*, "Activation of the ASTRO-E hard X-ray detector in low Earth orbit," *IEEE Transactions on Nuclear Science* **46**, 371–376 (1999).

201 D. E. Gruber, G. V. Jung, and J. L. Matteson, "Radioactivity observed in scintillation counters during the HEAO-1 mission," in *High-Energy Radiation Background in Space*, J. Rester, A. C. and J. I. Trombka, Eds., *American Institute of Physics Conference Series* **186**, 232–242 (1989).

202 C. Meegan, G. Lichti, P. N. Bhat, *et al.*, "The Fermi Gamma-ray Burst Monitor," *The Astrophysical Journal* **702**, 791–804 (2009).

203 A. Goldstein, "The Importance of Fermi GBM in the Era of Gravitational-Wave Astronomy," in *AAS/High Energy Astrophysics Division*, *AAS/High Energy Astrophysics Division* **17**, 203.04 (2019).

204 A. C. Collazzi, C. Kouveliotou, A. J. van der Horst, *et al.*, "The Five Year Fermi/GBM Magnetar Burst Catalog," *The Astrophysical Journal Supplement Series* **218**, 11 (2015).

205 N. Østgaard, T. Neubert, V. Reglero, *et al.*, "First 10 Months of TGF Observations by ASIM," *Journal of Geophysical Research (Atmospheres)* **124**, 14,024–14,036 (2019).

206 A. Ursi, M. Marisaldi, M. Tavani, *et al.*, "Detection of terrestrial gamma-ray flashes with the AGILE satellite," in *Journal of Physics Conference Series*, *Journal of Physics Conference Series* **841**, 012029 (2017).

207 T. Neubert, N. Østgaard, V. Reglero, *et al.*, "The asim mission on the international space station," *Space Science Reviews* **215**(2), 26 (2019).

208 D. Sarria, F. Lebrun, P.-L. Blelly, *et al.*, "TARANIS XGRE and IDEE detection capability of terrestrial gamma-ray flashes and associated electron beams," *Geoscientific Instrumentation, Methods and Data Systems* **6**, 239–256 (2017).

209 G. N. Pendleton, R. S. Mallozzi, W. S. Paciesas, *et al.*, "The Intensity Distribution for Gamma-Ray Bursts Observed with BATSE," *The Astrophysical Journal* **464**, 606 (1996).

210 W. S. Paciesas, C. A. Meegan, G. N. Pendleton, *et al.*, "The Fourth BATSE Gamma-Ray Burst Catalog (Revised)," *The Astrophysical Journal Supplement Series* **122**, 465–495 (1999).

211 G. N. Pendleton, J. Hakkila, and C. A. Meegan, "The BATSE trigger efficiency as a function of intensity and energy range," in *Gamma-Ray Bursts, 4th Hunstville Symposium*, C. A. Meegan, R. D. Preece, and T. M. Koshut, Eds., *American Institute of Physics Conference Series* **428**, 899–903 (1998).

212 C. Wigger, O. Wigger, E. Bellm, *et al.*, "Observation of an Unexpected Hardening in the Spectrum of GRB 021206," *The Astrophysical Journal* **675**, 553–565 (2008).

213 C. Wigger, W. Hajdas, A. Zehnder, *et al.*, "Spectral analysis of GRBs measured by RHESSI," *Nuovo Cimento B Serie* **121**, 1117–1121 (2006).

214 D. R. Willis, E. J. Barlow, A. J. Bird, *et al.*, "Evidence of polarisation in the prompt gamma-ray emission from GRB 930131 and GRB 960924," *Astronomy and Astrophysics* **439**, 245–253 (2005).

215 M. McConnell, D. Forrest, W. T. Vestrand, *et al.*, "Using BATSE to measure gamma-ray

burst polarization," in *Gamma-ray Bursts: 3rd Huntsville Symposium*, C. Kouveliotou, M. F. Briggs, and G. J. Fishman, Eds., *American Institute of Physics Conference Series* **384**, 851–855 (1996).